White Rose Research Online
eprints@whiterose.ac.uk
https://eprints.whiterose.ac.uk
Universities of Leeds, Sheffield and York

Deposited via The University of Leeds.

White Rose Research Online URL for this paper:
https://eprints.whiterose.ac.uk/id/eprint/218607/

Version: Accepted Version

Article:

Lyu, P., Luo, Q., Feng, G. et al. (2024) Development of an in-situ shaker for evaluating railway earthworks. Soil Dynamics and Earthquake Engineering, 179. 108550. ISSN: 0267-7261

https://doi.org/10.1016/j.soildyn.2024.108550

© 2024, Elsevier. This manuscript version is made available under the CC-BY-NC-ND 4.0 license http://creativecommons.org/licenses/by-nc-nd/4.0/. This is an author produced version of an article published in Soil Dynamics and Earthquake Engineering. Uploaded in accordance with the publisher's self-archiving policy.

Reuse
This article is distributed under the terms of the Creative Commons Attribution-NonCommercial-NoDerivs (CC BY-NC-ND) licence. This licence only allows you to download this work and share it with others as long as you credit the authors, but you can’t change the article in any way or use it commercially. More information and the full terms of the licence here: https://creativecommons.org/licenses/

Takedown
If you consider content in White Rose Research Online to be in breach of UK law, please notify us by emailing eprints@whiterose.ac.uk including the URL of the record and the reason for the withdrawal request.

UNIVERSITY OF LEEDS
University of Sheffield
UNIVERSITY of York

Development of an In-situ Shaker for Evaluating Railway Earthworks

Pengju Lyu
1. School of Civil Engineering, Southwest Jiaotong University, Chengdu 610031, China
E-mail: LvPengju@my.swjtu.edu.cn

Qiang Luo
1. School of Civil Engineering, Southwest Jiaotong University, Chengdu 610031, China;
2. Key Laboratory of High-speed Railway Engineering (Southwest Jiaotong University), Ministry of Education, Chengdu 610031, China
E-mail: LQrock@swjtu.edu.cn

Guishuai Feng
1. School of Civil Engineering, Southwest Jiaotong University, Chengdu 610031, China
E-mail: fgs@my.swjtu.edu.cn

David P. Connolly
3. School of Civil Engineering, University of Leeds, Leeds LS2 9JT, UK
Email: D.Connolly@leeds.ac.uk

Kaiwen Liu*
1. School of Civil Engineering, Southwest Jiaotong University, Chengdu 610031, China;
2. Key Laboratory of High-speed Railway Engineering (Southwest Jiaotong University), Ministry of Education, Chengdu 610031, China
E-mail: kaiwen.liu@queensu.ca (*Corresponding author)

Tengfei Wang
1. School of Civil Engineering, Southwest Jiaotong University, Chengdu 610031, China;
2. Key Laboratory of High-speed Railway Engineering (Southwest Jiaotong University), Ministry of Education, Chengdu 610031, China
E-mail: w@swjtu.edu.cn; ORCID: 0000-0003-4079-0687

Abstract

The geotechnical and geodynamic characteristics of railway earthworks under train loading are important quantities for railway and geotechnical engineers, but difficult to quantify. Characterizing the anticipated settlement and dynamic properties of compacted fills after earthwork construction, but before track laying, is advantageous, because modifying construction after laying the track is significantly more expensive. The difficulty in measuring these indices arises from the need to perform cyclic loading that realistically simulates the frequencies and magnitudes induced by trains. To address this issue, this paper introduces a novel shaker designed to apply cyclic loads similar to those of trains. The paper first presents an outline of the design requirements for the shaker, followed by the development of a theoretical dynamics model to aid mechanical design. This model is used for examining various shaker configurations, especially their performance under different potential testing conditions. The shaker's final design includes dual eccentric rotors that excite an adjustable-mass counterweight, complemented by a lateral support frame to counter horizontal movement and ensure vertical excitation. Once the shaker is built, it is used to evaluate newly constructed mudstone earthworks near a railway line. A method for estimating the dynamic stiffness and damping of earthworks is proposed, which uses data from frequency sweep test data from the shaker. Outputs from the dynamics model show close alignment with the field results. Finally, a method for designing the shaker configuration according to the desired loads is proposed.

Keywords: Railway Earthworks; Non-Destructive Testing; Dual-Rotor Shaker; Frequency Sweep; Fill Compaction

Nomenclature

C_Z, C_ψ	Damping coefficients in Z and ψ directions for the vibrating system
c_f	Damping coefficients of foundation per unit area
f	Frequency of electrical power supply
f'	Rotational frequency of eccentric rotors
f_N	Rated frequency of motor
f_i	Axis damping coefficients for motors, where $i = 1, 2$
g	Gravitational acceleration
J_a	Total moment of inertia of vibrating system about its center of mass
J_i	Combined moment of inertia of eccentric rotor and motor shaft
$J_{\mathrm{self},k}$	Individual moments of inertia for shaker components about their respective centers of mass
$J_{O',k}$	Moments of inertia for shaker components relative to the shaker's center of mass
J_M	Moment of inertia for shaker, excluding the eccentric rotors
J_{Oi}	Motor shaft's moments of inertia
K_z, K_ψ	Stiffness coefficients in Z and ψ directions for the vibrating system
k_f	Foundation stiffness coefficients per unit area
l	Distance from rotor's rotational center to shaker's center of mass
l_e	Distance between motor shafts
m_i	Mass of each eccentric rotor, where $i = 1, 2$
m	Mass of eccentric rotor when $m_1 = m_2$
m_e	Mass of an individual eccentric block
m_s	Mass of an individual counterweight block
M	Total mass of shaker, including motors, framework, loading plate, and counterweights
M_a	Combined mass of the vibrating system, inclusive of m_1 and m_2
n_e	Number of eccentric blocks on one end of a motor
n_s	Total number of counterweight blocks
n	Rotational speed of both the motor and the eccentric rotor (rpm)
n_0	Synchronous speed of motor (rpm)
n_N	Rated speed of motor (rpm)
P_N	Motor's rated power
p	Number of pole pairs in the motor
p_s	Induced stress under the loading plate on the foundation
p_v	Minimum value of p_s
$p_{\mathrm{p\text{-}v}}$	Peak-to-valley value of p_s
r	Eccentric rotor's radius
r_b	Radius of bottom of loading plate
s	Motor slip
s_N	Motor's rated slip
s_M	Motor's critical slip
s_M'	Critical slip after reducing motor's supply frequency
$T_{\mathrm{e}i}$	Electromagnetic torque generated by the motor, where $i = 1, 2$
T_M	Motor's maximum torque output
T_N	Motor's rated torque output
Z	Shaker's vertical displacement
α	Phase difference between the two eccentric rotors
α_m	Maximum absolute value of phase difference
α_MT	Motor's overload coefficient
β	Angle between line $O_\mathrm{i}O'$ and shaker's horizontal axis ($x'O'y'$)
β_a	Amplification multiplier
φ_i	Phase angle of eccentric rotor, where $i = 1, 2$
ψ	Shaker's swing angle
ω	Eccentric rotor's angular frequency

1. Introduction

Long-term, repeated train loading influences the stability and durability of railway substructures [1]. The cost of repairing earthworks after track installation can be considerable. Therefore, understanding the mechanical performance of these earthworks is crucial for optimizing the construction, operation, and maintenance economies of railway. Although wayside monitoring during train passage [2–4] provides useful insights, it can be costly and challenging to implement [5,6]. Mathematical models [1,7,8] and finite element methods [9–11] serve as cost-effective and convenient alternatives. However, these methods often involve simplifications and are dependent upon reliable input properties which are often difficult to measure [5,12,13].

An alternative approach is to use laboratory test platforms to simulate train loading on large-scale trackbed samples [14–16]. However, the challenge with this is the complex testing equipment required and boundary effects caused by the limited testing sample dimensions. Further, in a laboratory environment it can be difficult to construct track-earthwork test samples in the same manner as performed on-site. For example, large compaction plant can be challenging to operate in a laboratory space.

Considering the challenges with laboratory tests and numerical analysis, Miwa and Yoshimura [17] developed a vehicle-borne mechanical system which incorporated hydraulic actuators between the train and rail to serve as mechanical vibration shakers, simulating the vehicle's impact on the track structure. However, most alternative field shakers have employed inertial mechanisms to excite the track or earthworks, generating excitation through rotating eccentric rotors powered by electric motors. Wang [12] and Wang et al. [13], for instance, used an inertial shaker equipped with a drive system, circulating cooling system, and electric control system, to assess the dynamic performance of a novel structure tailored for expansive soil subgrade. Huang et al. [18] employed the same shaker to investigate the vibration characteristics of a ballasted railway subgrade supported by a pile-slab composite foundation [19,20]. Zhang et al. [21] applied an inertial excitation device to simulate the axial loads from a single bogie on an embankment filled with weathered red mudstone. Through excitation tests, the study evaluated the dynamic stresses, displacements, and accelerations of the railway track-subgrade system. In addition, Cai et al. [22] applied an inertial shaker which used a large volume of rectangular concrete as both base and counterweight to investigate the suitability of cement-improved expansive soil for use as fill material for heavy-haul railway subgrade. Ye et al. [23] employed a similar shaker to study the stress and deformation characteristics of a track-asphalt-concrete-subgrade system under varying temperature and train loading. While these shakers have found application in railway foundation research, most studies focus on stress and permanent deformation. Comprehensive analyses that include the dynamics of the entire system, comprising both the shaker and the foundation, as well as verification of the shaker’s output force, remain scarce.

Regarding mechanical shakers, extensive research has been performed on the different types of vibrating equipment, including vibrating screen systems [24], vibrating mills [25], and vibrating conveyors [26], among others [27–30]. These systems commonly employ a dynamic model simplified as a rigid mass block. This block is constrained by springs and dampers and is excited by the rotation of at least two eccentric rotors. The system's overall response is determined through a combination of theoretical, simulation, and experimental methods. Importantly, the shafts driving these eccentric rotors need not be mechanically interlinked through meshing gears. Under specific conditions, the rotor rotations can sustain a stable phase difference, thereby generating the necessary excitation for industrial applications. Consequently, the configuration may allow for the omission of a cooling system installed for the eccentric rotor connecting element employed by shakers in railway dynamic tests [12,21], offering a potential for cost savings. This research methodology coupled with the implementation of eccentric rotor arrangements without engagement, holds promise for the development of excitation equipment for railway applications.

Thus, this study introduces a design for a dual-rotor shaker optimized for the dynamic testing of railway earthworks. It is novel because it eliminates the need for meshing gears and other interconnections between eccentric rotors. The foundation is conceptualized as a damped spring, and Lagrange's equation is used to formulate differential equations that describe the dynamic behavior of the vibrating system. A simulation study is used to provide insights into the shaker's operational state and investigates the phase differences between the two eccentric rotors under differing potential testing conditions. A physical prototype, constructed according to the design, is used for in-situ tests on strongly weathered red-bed mudstone. A comparative analysis focuses on both the output stress generated by the shaker and the synchronization of its eccentric rotors, drawing upon test and simulation data. Additionally, this study proposes method for estimating soil stiffness and damping utilizing field test data, alongside technique for designing shaker configurations based on specific load requirements.

2. Design considerations

This section presents stress distribution characteristics in railway track foundations and addresses dynamic testing shaker design requirements. It concludes by presenting a concept shaker design.

2.1. Characteristics of train loading

Train loading is transferred to the foundation surface via the track structure. A typical stress-time curve of the track foundation surface is depicted in Fig. 1 [3,16,31]. The data is from the traversal of a train comprising two locomotives, positioned at each extremity, and six intermediate coaches, resulting in a total of 16 bogies and 32 axles [3,31]. Fig. 1a illustrates that for ballasted tracks, the number of peak stresses corresponds to the train's axle count. Fig. 1b demonstrates that for slab tracks, the number of peak stresses is equal to the bogie count. For ballasted and slab track foundation, the stress experienced during a single loading and unloading cycle is predominately implemented by an individual axle and bogie, respectively. This is caused by the increased bending stiffness of the concrete slab compared to the ballast. Depending upon the configuration of train, after several loading and unloading cycles, there may be a pause before the next one begins in the stress. Hence, the distribution of stress-time curves on track foundation surface due to train loading is influenced by several parameters. These include the car length, the distance between bogies, the axle spacing within bogies, the train speed, as well as track irregularities and the axle weight [8,32,33]. Furthermore, the dynamic loading of an actual train covers a broad frequency range [16,32].

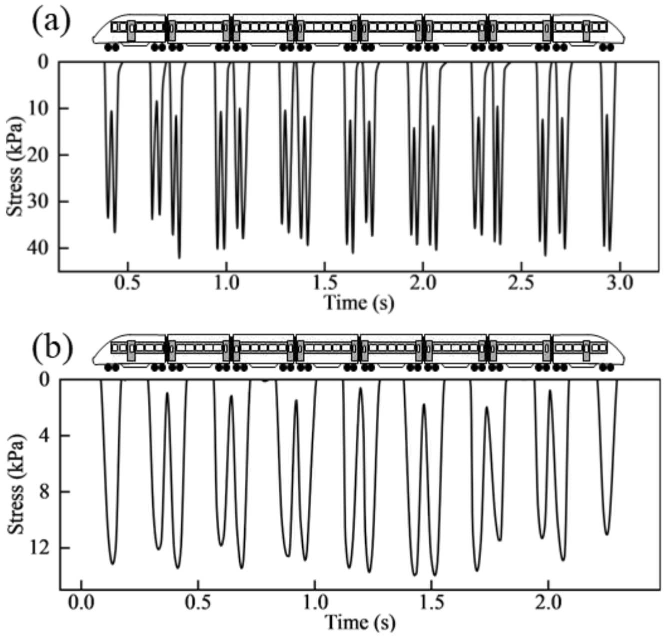

Fig. 1. Measured stress-time curve of the subgrade surface due to train loading for (a) ballasted track [3] and (b) slab track [16,31].

2.2. Design requirements for shaker loading

The stress produced in the track foundation by the train can be primarily boiled down to frequencies and amplitudes of stress [16,32]. The selection of specific frequency and amplitude depends on the potential operating scenarios of the railway earthworks under evaluation. In evaluating earthworks for both ballasted and slab track foundations, current shaker methods typically simulate train loading using harmonic excitation characterized by a single amplitude and frequency [12,13,18,21–23]. Fig. 2 illustrates a dynamic stress-time curve of a sinusoidal wave. Within the context of train loading simulation, the minimum stress reflects stress from the superstructure's self-weight, and maximum stress represents the total stress when train loading is considered. The difference between these, namely the peak-to-valley value, approximately simulates train loading. In addition to magnitude, load frequency also influences a structure's response. Specifically, when the load frequency aligns with the structure's natural frequency, this synchrony greatly amplifies the load's impact, potentially leading to a resonance phenomenon. This can severely compromise structural safety. Thus, it is crucial to account for load frequency while simulating the effects of train loading. The simple harmonic wave frequency is related to the speed of the train being simulated.

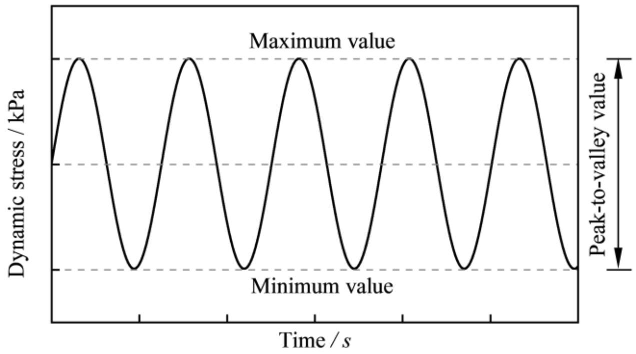

Fig. 2. Sinusoidal dynamic stress time curve.

Inertia-type shakers are commonly used to generate this type of harmonic loading. Using a shaker to produce consistent repeated loading for simulating train-induced stresses allows for accelerated testing and studying earthworks settlement. Additionally, employing the shaker to sweep across a spectrum of frequencies aids in assessing the dynamic properties of soil, involving stiffness and damping, which are crucial for setting parameters in numerical simulations [1,7,8]. Fig. 3 shows three inertial shakers used in railway earthwork research to produce cyclic loading.

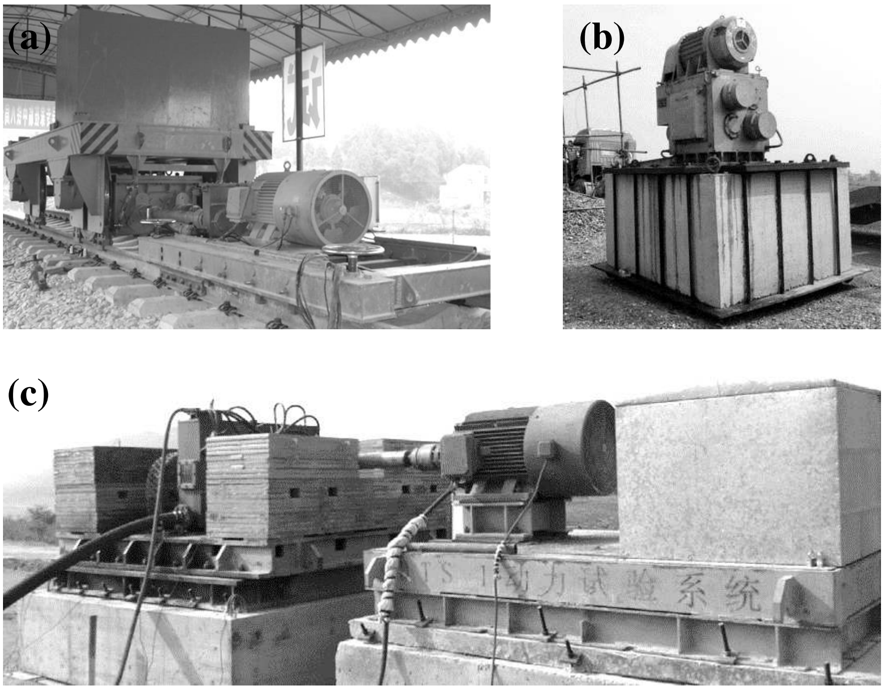

Fig. 3. Inertia-type shakers in railway earthwork dynamic testing: (a) ZSS50 [34];(b) SBZ60 [22]; (c) DTS-1 [12].

The *Code for Design of Railway Earth Structure* (TB10001-2016) stipulates that stresses on the track foundation surface due to the self-weight of the track range from 11.6 kPa to 14.3 kPa for slab tracks and 17.3 kPa to 23.3 kPa for ballasted tracks. In addition, the peak values of stresses on a slab track subgrade surface due to train loading generally range from 13 kPa to 20 kPa, while those for ballasted tracks vary between 50 kPa and 100 kPa [35]. The minimum value of the stress output from the shaker should at least match the self-weight of the track structure, with a minimum threshold of 11.6 kPa. Additionally, the peak-to-valley value of stress output from the shaker should surpass the train-induced stress, setting its minimum at no less than 13 kPa.

Studies available related to track foundation dynamics lack a definitive correlation between single-frequency loading and the frequency of train-induced loading. Zhang et al. [21] in their field experiments with the ZSS50 shaker (Fig. 3a) used a frequency of 15 Hz. Alternatively, Cai et al. [22] calculated the vibration frequency for dynamic tests with SBZ60 shaker (Fig. 3b) from the ratio of vehicle speed to axle spacing. Further, Wang [12] conducted a frequency sweep dynamic test on the subgrade, varying between 5~23 Hz with the DTS-1 shaker (Fig. 3c). Zhang [36] recommended using single-frequency loading at frequency that result in cumulative settlements identical to those caused by train loading. It may be viable to consider the dominant frequencies for the track foundation under a moving train as equivalent frequencies. Regarding slab track, the dominant frequencies are approximately 1.2 Hz and 3.6 Hz at a train speed of 108 km/h, around 2.4 Hz and 7.2 Hz for 216 km/h, and close to 4 Hz and 12 Hz for 360 km/h [16]. Based on the above studies, it is advised to design shakers capable of delivering loads at a maximum frequency of at least 25 Hz.

2.3. Initial design

Considering the typical characteristics of train and track loading, a novel conceptual model of a dual-rotor shaker for the dynamic testing of railway earthworks is shown in Fig. 4. It consists of two independent asynchronous electric motors mounted symmetrically on top of a counterweight structure, which drive eccentric blocks with equal mass, generating cyclic excitations. In contrast to the shakers depicted in Fig. 3, the uniqueness is the absence of mechanical coupling between the two motors, thus offering efficiencies in operation and maintenance. When the eccentric blocks, driven by the two motors, rotate in opposing directions at equal speeds, and the center of mass remains consistently symmetrical with respect to the plane between the two motors, synchronous rotation of the eccentric blocks is achieved. As a result of the eccentric block's synchronous rotation, a harmonic variation in the vertical direction of the resultant force is observed, while the horizontal direction maintains a null force, thus introducing harmonic excitation into the soil.

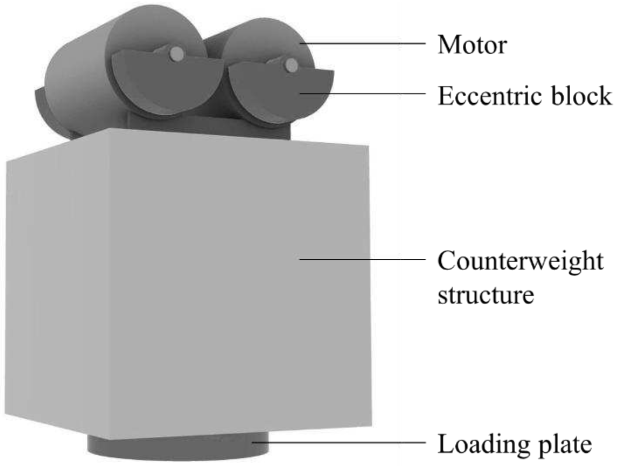

Fig. 4. Conceptual diagram of shaker.

The excitation of eccentric blocks is directly linked to their mass, eccentric radius, and rotation speed. Manufacturing eccentric blocks with a uniform shape is a practical approach and allows for the modulation of excitation intensity by changing the number of blocks engaged. The excitation intensity can also be changed by altering the supply frequency. The counterweight structure for the motors should have sufficient mass to counterbalance the upward force generated by the eccentric blocks, ensuring the shaker always remains in contact with the ground. Additionally, the mass of this structure must be variable to adjust the maximum and minimum values of the output force from the shaker. In addition, to effectively transfer the output force from the shaker to the soil, a loading plate may be situated beneath the counterweight structure. Ideally the design and configuration of the loading plate should be adaptable, allowing for alteration to match the required load distribution pattern. Incorporating variable-mass eccentric blocks and a counterweight structure, as well as a replaceable loading plate improves the equipment's adaptability.

3. Conceptual model

This section develops a conceptual mathematical model of the earthworks shaker, for the purposes of informing the mechanical system design. The methodology for determining parameters within this model is outlined. Subsequently, it explicates the application of explicit integration technique [37] in solving the relevant differential equations of the model. The explicit integration technique possesses both accuracy and efficiency in the resolution of nonlinear differential equations [1,7,38].

3.1. Dual-rotor shaker dynamics and foundation interaction

The general concept of the shaker is to use motor-driven eccentric blocks to excite a large counterweight to excite earthworks at a given frequency. Only vertical excitation is required meaning lateral displacement of the shaker must be minimised. Hence, Fig. 5 shows the dynamic model created for the shaker, focusing on the vertical displacement (Z) and swing angle (ψ) of the shaker and omitting horizontal displacement. The model incorporates two eccentric rotors, each with a specified eccentric radius r and mass m_i, rotating in opposite directions, where $i = 1,2$. All potential additional components (e.g. motors, counterweight structure, and loading plate) are considered as a unified rigid mass block with mass M. The instantaneous phase angle φ_i indicates the eccentric rotor's rotation relative to its center O_i. l represents the distance from point O_i to the mass center O' of shaker, and l_e is the separation between points O_i. The angle between line O_iO' and the horizontal axis of $x'O'y'$ affixed to the apparatus is signified by β. Finally, the foundation is modelled as a parallel spring system under the loading plate, influenced by viscous damping, with stiffness coefficients K_Z and K_ψ for the Z- and ψ- directions, respectively, along with damping coefficients C_Z and C_ψ.

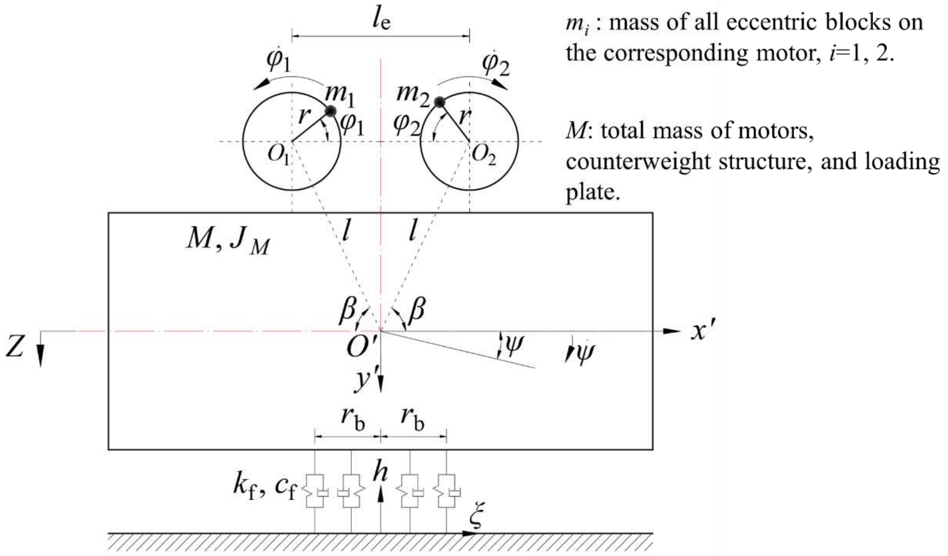

m_i : mass of all eccentric blocks on the corresponding motor, i=1, 2.

M: total mass of motors, counterweight structure, and loading plate.

Fig. 5. Dynamic model of dual-rotor shaker.

The coordinate axis ξ perpendicular to the motor shaft originates at the center of the lower surface of loading plate, as illustrated in Fig. 5. The coordinates for points on the loading plate sharing the same elevation with the non-displaced horizontal foundation surface are calculated as $\xi_c = -Z/\psi$, based on instantaneous values of Z and ψ. ξ_c enables real-time updates to K_Z, K_ψ, C_Z and C_ψ. Subsequently, non-linear interaction between the foundation surface and the shaker base can be considered. As an example, the circular loading plate with radius r_b shown in Fig. 6 will be used to illustrate how to update K_Z, K_ψ, C_Z and C_ψ based on the ξ_c values.

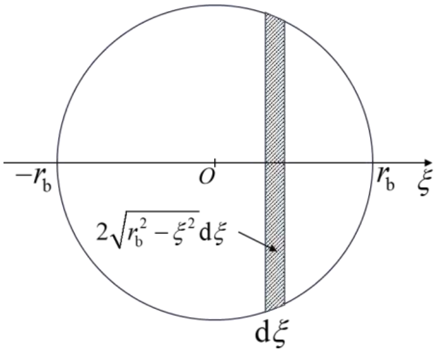

Fig. 6. Coordinate axis representation on circular loading plate bottom.

The parallel spring assembly representing the foundation under the shaker's base exhibits stiffness k_f

and damping c_f per unit area. The shaded region depicted in Fig. 6 represents the loading plate's area within the interval $[\xi, \ \xi+\mathrm{d}\xi]$, measuring $2\sqrt{r_\mathrm{b}^2-\xi^2}\mathrm{d}\xi$. The equivalent stiffness and damping of the foundation with shaded area in contact with the loading plate are $2k_\mathrm{f}\sqrt{r_\mathrm{b}^2-\xi^2}\mathrm{d}\xi$ and $2c_\mathrm{f}\sqrt{r_\mathrm{b}^2-\xi^2}\mathrm{d}\xi$, respectively. In the scenario where $\psi \geq 0$ (or $\psi < 0$), the shaker maintains contact with the substrate, corresponding to $\xi_\mathrm{c} < -r_\mathrm{b}$ (or $\xi_\mathrm{c} > r_\mathrm{b}$). Here, K_Z, K_ψ, C_Z and C_ψ are determined according to Eq. (1). In instances where partial separation occurs between the shaker base and the foundation surface, corresponding to $-r_\mathrm{b} \leq \xi_\mathrm{c} \leq r_\mathrm{b}$, Eq. (1) is modified by adjusting the lower (or upper) integration limits to ξ_c for ascertaining K_Z, K_ψ, C_Z and C_ψ accurately. In cases of complete separation, denoted by $\xi_\mathrm{c} > r_\mathrm{b}$ (or $\xi_\mathrm{c} < -r_\mathrm{b}$), all these parameters reset to zero.

$$\begin{cases} K_Z = 2k_\mathrm{f}\int_{-r_b}^{r_b}\sqrt{r_b^2-\xi^2}\,d\xi \\ K_\psi = 2k_\mathrm{f}\int_{-r_b}^{r_b}\xi^2\sqrt{r_b^2-\xi^2}\,d\xi \\ C_Z = 2c_\mathrm{f}\int_{-r_b}^{r_b}\sqrt{r_b^2-\xi^2}\,d\xi \\ C_\psi = 2c_\mathrm{f}\int_{-r_b}^{r_b}\xi^2\sqrt{r_b^2-\xi^2}\,d\xi \end{cases} \tag{1}$$

3.2. Equations of motion

The coordinates of the two eccentric rotors within the $x'O'y'$ coordinate system can be expressed using Eq. (2).

$$\begin{cases} \Phi_1' = \begin{bmatrix} -l\cos\beta + r\cos\varphi_1 \\ -l\sin\beta - r\sin\varphi_1 \end{bmatrix} \\ \Phi_2' = \begin{bmatrix} l\cos\beta - r\cos\varphi_2 \\ -l\sin\beta - r\sin\varphi_2 \end{bmatrix} \end{cases} \tag{2}$$

In the $x'O'y'$ coordinate system, which is integral to the oscillating mechanism, real-time motion occurs along the Z- and ψ-directions. The transformation relations outlined in Eq. (3) clarify the spatial coordinates of the eccentric rotors within the fixed coordinate system, culminating in the formulation presented in Eq. (4).

$$\Phi_i = \begin{bmatrix} 0 \\ Z \end{bmatrix} + \begin{bmatrix} \cos\psi & -\sin\psi \\ \sin\psi & \cos\psi \end{bmatrix} \Phi_i' \tag{3}$$

$$\begin{cases} \Phi_1 = \begin{bmatrix} -l\cos(\beta+\psi) + r\cos(\varphi_1 - \psi) \\ Z - l\sin(\beta+\psi) - r\sin(\varphi_1 - \psi) \end{bmatrix} \\ \Phi_2 = \begin{bmatrix} l\cos(\beta-\psi) - r\cos(\varphi_2 + \psi) \\ Z - l\sin(\beta-\psi) - r\sin(\varphi_2 + \psi) \end{bmatrix} \end{cases} \tag{4}$$

Eq. (5) defines the kinetic energy T of the system:

$$T = \frac{1}{2} M\dot{Z}^2 + \frac{1}{2} J_M \dot{\psi}^2 + \frac{1}{2}\sum_{i=1}^{2} J_{Oi}\dot{\varphi}_i^2 + \frac{1}{2}\sum_{i=1}^{2} m_i \dot{\Phi}_i^T \dot{\Phi}_\mathrm{i} \tag{5}$$

where J_M signifies the moments of inertia of the rigid frame around its mass center, while J_{0i} represents the shaft's inertia moments of motor i, i=1, 2.

In the system, the natural positions of the springs serve as zero potential energy reference points for both elastic and gravitational fields. Eq. (6) formulates the total potential energy U:

$$U = \frac{1}{2} K_Z Z^2 + \frac{1}{2} K_\psi \psi^2 - M_\mathrm{a} g Z \tag{6}$$

where $M_\mathrm{a}=M+m_1+m_2$ and acceleration of gravity g of 9.8 m/s^2 is assumed.

The viscous dissipation function D, originating from the energy exchange in the springs and motor shaft friction, is presented in Eq. (7):

$$D = \frac{1}{2} C_Z \dot{Z}^2 + \frac{1}{2} C_\psi \dot{\psi}^2 + \frac{1}{2} f_1 \dot{\varphi}_1^2 + \frac{1}{2} f_2 \dot{\varphi}_2^2 \tag{7}$$

where f_1 and f_2 stand for the axis damping coefficients for the induction motors driving eccentric rotors 1 and 2, respectively.

The system's generalized coordinates are shown in Eq. (8), while Eq. (9) defines the generalized force matrix. Here, $T_{\mathrm{e}1}$ and $T_{\mathrm{e}2}$ represent the electromagnetic torques driving eccentric rotors 1 and 2, respectively.

$$\mathbf{q} = [Z \quad \psi \quad \varphi_1 \quad \varphi_2] \tag{8}$$

$$\mathbf{P} = [0 \quad 0 \quad T_{\mathrm{e1}} \quad T_{\mathrm{e2}}] \tag{9}$$

Finally, the generalized Lagrange's equation [27] as expressed in Eq. (10) is used to establish the system's dynamic differential equations.

$$\frac{\mathrm{d}}{\mathrm{d}t}\left(\frac{\partial(T-U)}{\partial\dot{\mathbf{q}}}\right) - \frac{\partial(T-U)}{\partial\mathbf{q}} + \frac{\partial D}{\partial\dot{\mathbf{q}}} = \mathbf{P} \tag{10}$$

In mechanical vibration studies, it is commonly observed that $\psi \ll 1$ [27,39]. This allows the approximations sin $\psi \approx 0$ and cos $\psi \approx 1$ when expanding the dynamic equations obtained by substituting Eqs. (4) through (9) into Eq. (10). Subsequently, in the dynamic model where $m_i \ll M$, the equation of motion for the system is derived as shown in Eq. (11), following the further simplification of the expanded dynamic equations based on references [27,39,40]:

$$\begin{cases} M_{\mathrm{a}}\ddot{Z} + C_Z\dot{Z} + K_Z Z + r\sum_{i=1}^{2} m_i(\dot{\varphi}_i^2 \sin\varphi_i - \ddot{\varphi}_i \cos\varphi_i) = M_{\mathrm{a}} g \\ J_{\mathrm{a}}\ddot{\psi} + C_\psi\dot{\psi} + K_\psi\psi + r\sum_{i=1}^{2}(-1)^i m_i[\dot{\varphi}_i^2 l \sin(\varphi_i + \beta) + \ddot{\varphi}_i(r - l\cos(\varphi_i + \beta))] = 0 \\ J_1\ddot{\varphi}_1 + f_1\dot{\varphi}_1 \\ +m_1 r[-\ddot{Z}\cos\varphi_1 - \dot{\psi}^2 l \sin(\varphi_1 + \beta) - \ddot{\psi}(r - l\cos(\varphi_1 + \beta))] = T_{\mathrm{e1}} \\ J_2\ddot{\varphi}_2 + f_2\dot{\varphi}_2 \\ +m_2 r[-\ddot{Z}\cos\varphi_2 - \dot{\psi}^2 l \sin(\varphi_2 + \beta) + \ddot{\psi}(r - l\cos(\varphi_2 + \beta))] = T_{\mathrm{e2}} \end{cases} \tag{11}$$

where, $J_{\mathrm{a}}=J_M + \Sigma m_i(r^2+l^2)$, and $J_i=J_{Oi}+m_i r^2$, i=1,2.

Upon substituting the slip s as shown in Eq. (12), into Eq. (13) for torque T_{e}, the mathematical relation between T_{e} and the rotational speed n of the three-phase asynchronous can be defined as shown in Eq. (14) [41]:

$$s=\frac{n_0-n}{n_0} \tag{12}$$

$$T_e=\frac{2T_M}{\frac{s}{s_M}+\frac{s_M}{s}} \tag{13}$$

$$T_e=\frac{2T_M s_M n_0 (n_0-n)}{s_M^2 n_0^2+(n_0-n)^2} \tag{14}$$

where n_0 denotes the synchronous speed of the motor. T_M signifies the maximum torque output of the vibratory motor, which is mathematically defined as $T_M=\alpha_{MT}T_N$. α_{MT} denotes the overload coefficient of the motor and $T_N=(60P_N)/(2n_N\pi)$ presents the rated torque, while P_N and n_N represent the rated power and rotational speed of the motor, respectively. Moreover, $s_M=s_N(\alpha_{MT}+\sqrt{\alpha_{MT}^2-1})$ characterizes the critical slip of the motor, while s_N represents the rated slip ratio of the vibratory motor.

Upon reducing the power supply frequency of a vibration motor with a rated frequency f_N of 50 Hz for variable-speed control, the power supply frequency transitions to f ($f\leq f_N$), with the variable T_M remaining unaltered. Substituting f into Eq. (15) and taking into account the number of pole pairs p present in the stator, n_0 can be recalibrated. Similarly, the critical slip becomes inversely related to the altered supply frequency, necessitating an update to s_M' as dictated by Eq. (16) [41]. Insertion of $n_i=30\dot{\varphi}_i/\pi$ into Eq. (14) allows for the calculation of the instantaneous electromagnetic torque T_{ei}, i=1, 2, within the framework of the dynamic differential equations established in Eq. (11).

$$n_0=\frac{60f}{p} \tag{15}$$

$$s_M{}'=\frac{f_N}{f}s_M \tag{16}$$

3.3. Simulation parameters

To define the variables shown in Fig. 5, the mass of system must be known. Each single eccentric block has a mass m_e and the individual counterweight block have a mass m_s. The mass m_i of each eccentric rotor (where i=1, 2) is modulated by altering the number of eccentric blocks n_e at each end of the motor. The shaker mass M encompasses the motors, counterweight structure, and loading plate, which are modulated by adjusting the quantity n_s of counterweight blocks. The masses m_i is computed in accordance with Eq. (17). Similarly, the mass M_s of counterweights is calculated using Eq. (18).

$$m_i = 2n_\mathrm{e}m_\mathrm{e} \tag{17}$$

$$M_\mathrm{s} = n_\mathrm{s}m_\mathrm{s} \tag{18}$$

Owing to the system's bilateral symmetry, O' aligns with the central axis of symmetry. The elevation $\bar{h}$ of O' relative to the bottom of shaker complies with Eq. (19).

$$\bar{h} = \frac{\sum M_k h_k}{\sum M_k} \tag{19}$$

Here, M_k denotes the mass of each component of the shaker while h_k is the height of the centre of mass for each part of the shaker relative to the bottom of shaker.

The separation between the two motor shafts is l_e, while the vertical elevation of the motor shaft from the bottom of shaker is denoted by h_1. Using Eq. (20), the distance l shown in Fig. 5 can be obtained.

$$l = \sqrt{(h_1 - \bar{h})^2 + (l_\mathrm{e}/2)^2} \tag{20}$$

Eq. (21) provides the means to ascertain the angle β shown in Fig. 5.

$$\beta = \arctan\frac{h_1 - \bar{h}}{l_\mathrm{e}/2} \tag{21}$$

The moment of inertia for a rigid body serves as a metric for its rotational inertia, dependent upon both mass magnitude and spatial distribution. To facilitate computation, the various components of the shaker can be simplified into geometric bodies with regular shape and uniform mass distribution. For example, the vibratory motors and a circular loading plate can be modeled as homogeneous cylinders, while some other components can be generalized as cuboids. Their moments of inertia about their respective centroids ($J_{\mathrm{self},\,k}$) can be easily obtained.

Using Eq. (22), the moments of inertia $J_{O',k}$ for each component of the shaker, relative to the centre of mass O' of the shaker, are:

$$J_{O',k} = J_{\mathrm{self},k} + M_k d_k^{\,2} \tag{22}$$

where d_k^2 specifies the square of distance between the centroid of each component and O'.

The moment of inertia J_M of the shaker is subsequently derived by summing the individual moments of inertia, each relative to O', as stipulated by Eq. (23).

$$J_M = \sum J_{O',k} \tag{23}$$

3.4. Numerical solutions

To streamline the solution process, the differential equations governing the shaker vibration are arranged in matrix form, as shown:

$$[M]\{\ddot{X}\} + [C]\{V\} + [K]\{X\} = [P] \tag{24}$$

where the constituent elements of the matrices and vectors are elaborated upon in Eqs. (25) through (31).

$$\{X\} = \{Z \;\; \psi \;\; \varphi_1 \;\; \varphi_2\}^{\mathrm{T}} \tag{25}$$

$$\{V\} = \{\dot{Z} \;\; \dot{\psi}^2 \;\; \dot{\varphi}_1^{\,2} \;\; \dot{\varphi}_2^{\,2}\}^{\mathrm{T}} \tag{26}$$

$$\{\ddot{X}\} = \{\ddot{Z} \;\; \ddot{\psi} \;\; \ddot{\varphi}_1 \;\; \ddot{\varphi}_2\}^{\mathrm{T}} \tag{27}$$

$$[M]=\begin{bmatrix} M_{\mathrm{a}} & 0 & -m_1 r\cos\varphi_1 & -m_2 r\cos\varphi_2 \\ 0 & J_{\mathrm{a}} & -m_1 r(r-l\cos(\varphi_1+\beta)) & m_2 r(r-l\cos(\varphi_2+\beta)) \\ -m_1 r\cos\varphi_1 & -m_1 r(r-l\cos(\varphi_1+\beta)) & J_1 & 0 \\ -m_2 r\cos\varphi_2 & m_2 r(r-l\cos(\varphi_2+\beta)) & 0 & J_2 \end{bmatrix} \tag{28}$$

$$[C]=\begin{bmatrix} C_Z & 0 & m_1 r\sin\varphi_1 & m_2 r\sin\varphi_2 \\ 0 & 0 & -m_1 rl\sin(\varphi_1+\beta) & m_2 rl\sin(\varphi_2+\beta) \\ 0 & -m_1 rl\sin(\varphi_1+\beta) & 0 & 0 \\ 0 & -m_2 rl\sin(\varphi_2+\beta) & 0 & 0 \end{bmatrix} \tag{29}$$

$$[K]=\begin{bmatrix} K_Z & 0 & 0 & 0 \\ 0 & K_\psi & 0 & 0 \\ 0 & 0 & 0 & 0 \\ 0 & 0 & 0 & 0 \end{bmatrix} \tag{30}$$

$$[P]=[M_{\mathrm{a}}g \quad -C_\psi\dot{\psi} \quad T_{\mathrm{e}1}-f_1\dot{\varphi}_1 \quad T_{\mathrm{e}2}-f_2\dot{\varphi}_2]^{\mathrm{T}} \tag{31}$$

An explicit integration method [37] was employed to solve the differential equations of motion for the vibrating system. The integration scheme of this approach is outlined in Eq. (32).

$$\begin{cases} \{X\}_{st+1}=\{X\}_{st}+\{\dot{X}\}_{st}\Delta t+(1/2+\psi_{\mathrm{int}})\{\ddot{X}\}_{st}\Delta t^2-\psi_{\mathrm{int}}\{\ddot{X}\}_{st-1}\Delta t^2 \\ \{\dot{X}\}_{st+1}=\{\dot{X}\}_{st}+(1+\varphi_{\mathrm{int}})\{\ddot{X}\}_{st}\Delta t-\varphi_{\mathrm{int}}\{\ddot{X}\}_{st-1}\Delta t \end{cases} \tag{32}$$

Here, Δt denotes the time step and was selected as 10^{-3} s for solving the shaker's dynamic equations. φ_{int} and ψ_{int}, set at 0.5, regulate the algorithm's stability and precision. The subscript '*st*' marks the current integration step. The vector $\{\dot{X}\}$ results from the temporal first-order derivative of $\{X\}$, defined as $\{\dot{X}\}=\{\dot{Z} \ \dot{\psi} \ \dot{\varphi}_1 \ \dot{\varphi}_2\}^{\mathrm{T}}$. Special attention was given to managing the transformation between $\{\dot{X}\}$ and $\{V\}$ throughout the solution process.

Incorporation of initial conditions into Eq. (24) yields Eq. (33), which defines the system's initial acceleration. For the initialization of the integration procedure, the terms φ_{int} and ψ_{int} are set to zero at the first-time step. Eq. (32) then facilitates the computation of the subsequent system displacements and velocities.

$$\left\{\ddot{X}\right\}_0 = [M]_0^{-1}([P]_0 - [K]_0\{X\}_0 - [C]_0\{V\}_0) \tag{33}$$

Further, integrating Eq. (32) into Eq. (24) produces Eq. (34), which defines the state of the system at (st+1)×Δt.

$$[M]_{st+1}\{\ddot{X}\}_{st+1} + [C]_{st+1}\{V\}_{st+1} + [K]_{st+1}\{X\}_{st+1} = [P]_{st+1} \tag{34}$$

And then, this computation evolves into Eq. (35):

$$\{\ddot{X}\}_{st+1} = [M]_{st+1}^{-1}\{\tilde{P}\}_{st+1} \tag{35}$$

with

$$\{\tilde{P}\}_{st+1} = [P]_{st+1} - \left[K\right]_{st+1}\{X\}_{st+1} - \left[C\right]_{st+1}\{V\}_{st+1}$$

In summary, iterative application of Eq. (32) and Eq. (35) enable the calculation of the discrete values for displacement, velocity, and acceleration at each time step, culminating in the numerical solution of the system.

4. Virtual development

This section introduces the general mechanical design of the shaker. Next the dynamic behavior of it across three operational states is investigated. Then the influence of potential experimental variable uncertainties on the synchronous operation of the shaker's eccentric rotors is studied.

4.1. Generalised mechanical design

A generalised mechanical design for the shaker was developed as depicted in Fig. 7. As shown in Fig. 7a, the device features two, three-phase asynchronous motors, each fitted with a maximum of 10 eccentric blocks at one end. These motors are symmetrically mounted on an internal frame designed to accommodate counterweights. Adjacent to the internal frame's steel columns, an external frame equipped with rubber wheels ensures stability while permitting operational clearance. Fig. 7b provides a detailed frontal view that identifies the various components of the apparatus. Motor speed control is managed through a frequency modulator connected to a 380 V, 50 Hz AC power supply. The internal frame dimensions are 600 mm × 600 mm × 590 mm and comprise three horizontal layers of rectangular steel plates, fortified by 11 vertical columns. This design creates eight zones for counterweight placement, each capable of accommodating up to 25 rectangular counterweights measuring 215 mm × 285 mm × 10 mm. A loading plate at the base of the internal frame is composed of two concentric, welded circular steel plates. The top plate measures 400 mm in diameter and 10 mm in thickness, while the bottom plate has a diameter of 300 mm and a thickness of 25 mm.

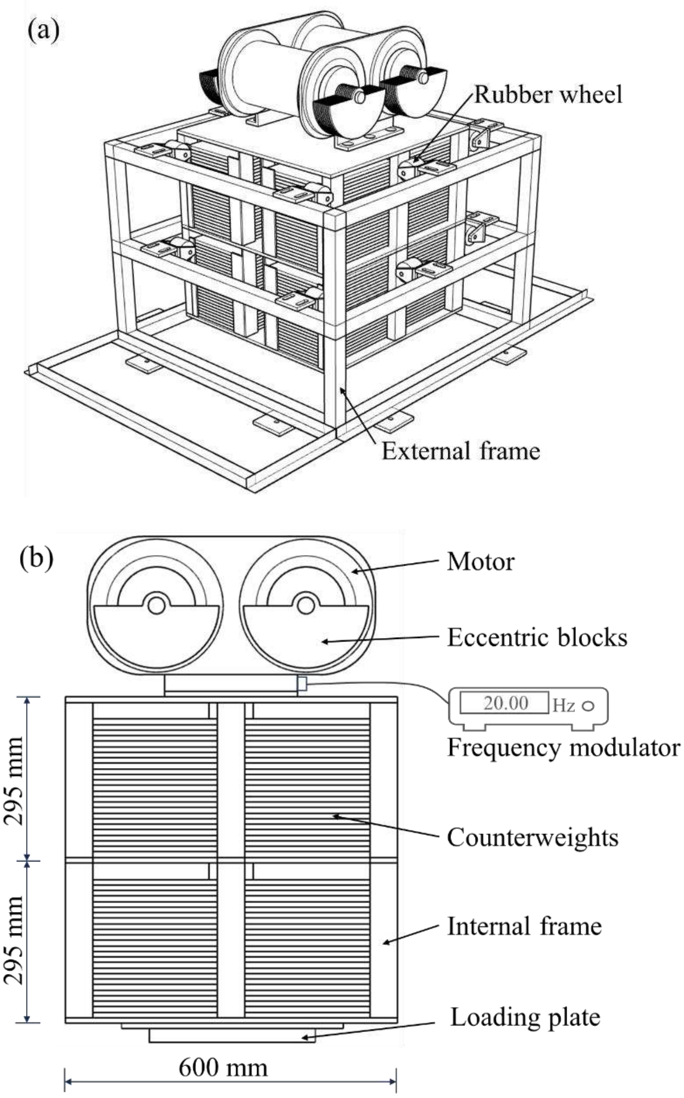

Fig. 7. Dual-rotor shaker design schematic: (a) perspective view; (b) front view.

Fig. 8 illustrates the inner framework for placing the counterweight blocks. As shown in Fig. 8a, the internal frame is segmented into 9 sections, identified as a to i. Sections a, b, and c correspond to three horizontal steel plates. The steel columns aligned identically in the frontal perspective are classified into six groups, from d to i. The mass of each column group is equally apportioned across the surface of the foremost plate. Likewise, the counterweights, identified from I to IV, have their masses evenly distributed across the areas of their front views. This approach simplifies the spatially non-uniform distribution of the internal frame and counterweight blocks into blocks with uniform mass distributions as depicted in Fig. 8b. This facilitates the calculation of the shaker's center of mass (O') and its moment of inertia (J_M). In practice, priority is placed on the equitable distribution of counterweights across the four pre-defined lower regions. Upon n_s being greater than the maximum quota of 100 for these lower zones, surplus counterweights are equally deployed in the upper regions.

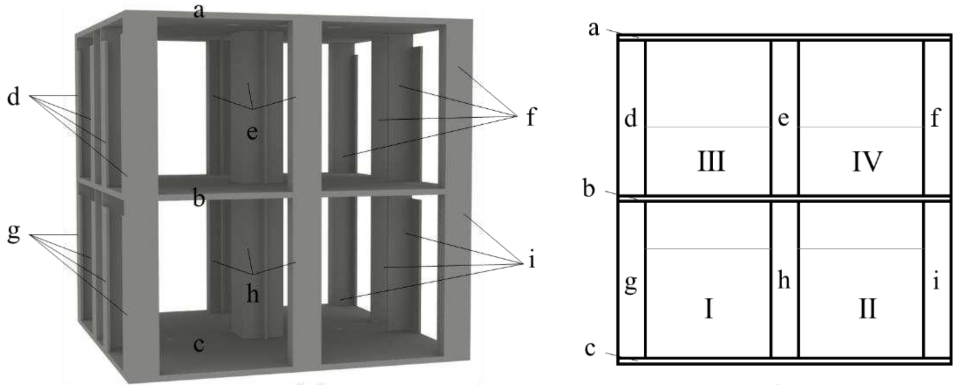

(a) (b)

Fig. 8. Internal frame and counterweight division: (a) internal frame zoning; (b) schematic of the mass distribution.

Each eccentric block has a mass m_e of 889.11 g and an eccentricity radius r of 46 mm. The inner framework has a mass of 124.5 kg. Individual counterweight block has a mass m_s of 4.5 kg. The steel plate in the upper section of the loading plate weighs 9.9 kg, while its lower counterpart has a mass of 13.8 kg. Excluding the eccentric blocks, the mass of each vibrating motor is 75 kg. The separation between the two motor shafts (l_e) is 0.27 m. The component specifications for calculating the mass center coordinates, moment of inertia of the shaker, and other parameters according to the methodology in Section 3.3 are given in Table 1. In the formula for d_k^2 within Table 1, the first term represents the square of the horizontal distance between the center of mass of the component in row and the shaker's center of mass. The second term accounts for the square of the vertical distance between these two centers of mass. In addition, the parameters for counterweights listed in Table 1 are calculated based on whether the number of counterweight blocks (n_s) is greater than 100. For $n_s \leq 100$, the parameters are defined as follows: $M_{12} = M_{13} = M_s/2$, $M_{14} = M_{15} = 0$, $h_{12} = h_{13} = 0.045+0.01n_s/8$, $J_{\mathrm{self},12} = J_{\mathrm{self},13} = M_{12}(0.285^2+(0.01n_s/4)^2)/12$, and $J_{\mathrm{self},14} = J_{\mathrm{self},15} = 0$. Conversely, for $n_s > 100$, the parameters are adjusted as follows: $M_{12} = M_{13} = 100m_s/2$, $M_{14} = M_{15} = (n_s-100)m_s/2$, $h_{12} = h_{13} = 0.045+0.01\times100/8$, $h_{14} = h_{15} = 0.335+0.01(n_s-100)/8$, $J_{\mathrm{self},12} = J_{\mathrm{self},13} = M_{12}(0.285^2+(0.01\times100/4)^2)/12$, and $J_{\mathrm{self},14} = J_{\mathrm{self},15} = M_{14}(0.285^2+(0.01\times(n_s-100)/4)^2)/12$.

Table 1. Component specifications of the shaker

Components		No. k	M_k (kg)	h_k (m)	$J_{\mathrm{self},\,k}$ (kg·m^2)	d_k^2 (m^2)
Motor 1		1	75.0	0.790	0.304	$0.135^2+(h_1-\bar{h})^2$
Motor 2		2	75.0	0.790	0.304	$0.135^2+(h_2-\bar{h})^2$
Internal frame	a	3	28.3	0.620	0.8492	$0^2+(h_3-\bar{h})^2$
	b	4	28.3	0.330	0.8492	$0^2+(h_4-\bar{h})^2$
	c	5	28.3	0.040	0.8492	$0^2+(h_5-\bar{h})^2$
	d	6	5.5	0.475	0.0371	$0.275^2+(h_6-\bar{h})^2$
	e	7	8.8	0.475	0.0593	$0^2+(h_7-\bar{h})^2$
	f	8	5.5	0.475	0.0371	$0.275^2+(h_8-\bar{h})^2$
	g	9	5.5	0.185	0.0371	$0.275^2+(h_9-\bar{h})^2$
	h	10	8.8	0.185	0.0593	$0^2+(h_{10}-\bar{h})^2$
	i	11	5.5	0.185	0.0371	$0.275^2+(h_{11}-\bar{h})^2$

Counterweights	I	12	M_{12}	h_{12}	$J_{\mathrm{self},12}$	$0.149^2+(h_{12}-\bar{h})^2$
	II	13	M_{13}	h_{13}	$J_{\mathrm{self},13}$	$0.149^2+(h_{13}-\bar{h})^2$
	II	14	M_{14}	h_{14}	$J_{\mathrm{self},14}$	$0.149^2+(h_{14}-\bar{h})^2$
	IV	15	M_{15}	h_{15}	$J_{\mathrm{self},15}$	$0.149^2+(h_{15}-\bar{h})^2$
Loading plate	Upper plate	16	9.9	0.030	0.0991	$0^2+(h_{16}-\bar{h})^2$
	Lower plate	17	13.8	0.0125	0.0783	$0^2+(h_{17}-\bar{h})^2$

The parameters for the vibratory motors are shown in Table 2. The motor's rotational speed n indicates its revolutions per minute, whereby the rotation frequency, f', is calculated as n divided by 60 seconds. Initial simulations showed that n closely approximates the synchronous speed n_0 as defined by Eq. (15). Thus, approximating n to be equivalent to n_0, then f' is derived as the quotient of $60f/p$ and 60 seconds. Hence, the rotation frequency f' of the eccentric rotors powered by the shaker's motors, characterized by two pole pairs, is approximated as $f/2$. The shaker generates excitation through the combined action of two eccentric rotors rotating at a frequency denoted by f'. When these rotors operate in synchronization, the excitation frequency of the shaker matches f'. The two vibration motors, having a rated frequency (f_N) of 50 Hz, may generate excitations up to a maximum frequency of 25 Hz and a peak force of 40 kN.

Table 2. Vibration motor parameters

Parameters	Symbols	Units	Values
Inertia moments of motor shaft	J_0	kg·m^2	0.018
Number of pole pairs	p	-	2
Rated power	P_N	W	1 100
Rated rotational speed	n_N	rpm	1 462
Rated torque	T_N	N·m	7.18
Rated frequency	f_N	Hz	50 Hz
Rated slip	s_N	-	0.025 3
Motor overload coefficient	α_{MT}	-	2.5
Axis damping coefficient of the induction motor	f_i	N·m·s/rad	1×10^{-6}

4.2. System behavior

This section outlines the system's behavior when the shaker's two eccentric rotors function synchronously, either maintaining or losing contact between the base of shaker and the foundation surface. It then examines a potential scenario where the rotors rotate asynchronously while the base stays in contact with the foundation. These classical cases are presented primarily to study the relationship between the eccentric rotor's phase difference and the shaker's operating state.

Fig. 9 shows the vibrating system's dynamic behavior under the conditions: k_f=251.0 MPa/m, c_f=868.3 kPa·s/m, n_s=200, n_e=1, f=32 Hz, along with two equal-weight eccentric rotors in the simulation. Initial conditions are $\varphi_1=\varphi_2=-90°$, denoting the eccentric rotors' alignment beneath the motor shaft, and ψ=0, indicating a level foundation surface. Fig. 9a demonstrates that the phase difference α between the dual eccentric rotors calculated by $\varphi_1-\varphi_2$ remains invariant at zero, thereby ensuring synchronized rotation. This synchronicity leads to the generation of forces exclusively in the vertical direction, nullifying any horizontal force components. Further, the shaker displacement along the ψ-axis remains negligible, as confirmed by Fig. 9a. Fig. 9b which shows synchronized rotation elicits a vertical dynamic displacement Z ranging from 0.47 mm to 0.86 mm, correlating with stress p_s on the foundation under the loading plate of between 117 and 216 kPa. p_s is calculated as the total force at the base of the loading plate divided by its bottom area. This total force is determined by summing the products of vertical displacement and stiffness (k_f) per unit area within the contact area between loading plate and ground. The persistent positive displacement and uninterrupted soil loading confirm no detachment of the shaker base from the foundation. It is important to note that the black or grey regions depicted in Fig. 9b and other similar illustrations represent tightly bunched cycles. Detailed cycle traces are seen in the magnified sections within the figure.

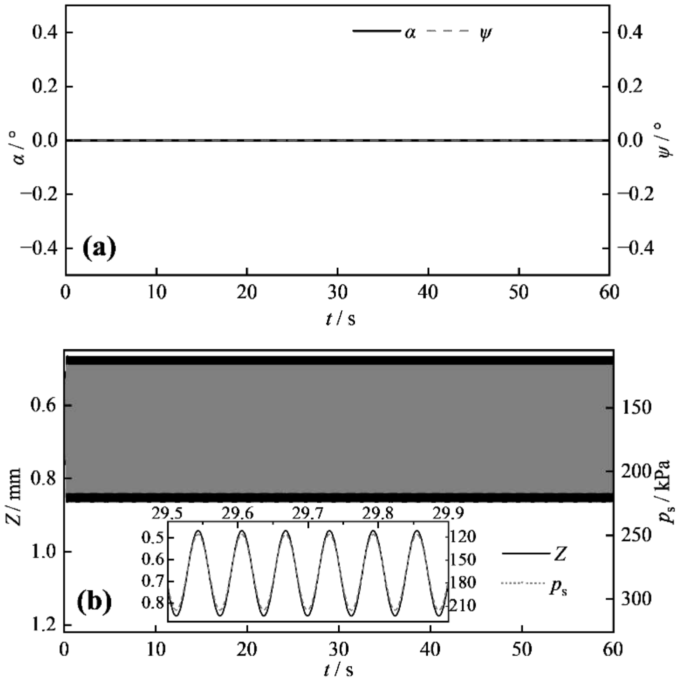

Fig. 9. System behavior of ground-attached shaker with eccentric rotors synchronization: (a) α and ψ; (b) Z and p_s.

Changing n_e to 5, as based on the system configuration of Fig. 9, yields the dynamic response depicted in Fig. 10. Fig. 10a confirms continuous synchronized rotation of the eccentric rotors, negating any ψ-direction displacement. Fig. 10b shows that Z spans from −1.50 mm to 2.17 mm, corresponding to p_s ranging from 0 to 540 kPa. The augmented rotor mass amplifies the dynamic excitations, thereby broadening the range of both displacement and stress in Fig. 9b. Notably, the negative minimum displacement and null stress signify that detachment of the shaker base from the foundation occurs during the shaker's operation. In addition, the contact state between the shaker and foundation is determined by the combined effects of the Z- and ψ-directed motions. However, a minima of zero for a single parameter p_s can serve as a definitive indicator of their detachment. Consequently, checking whether p_s is less than zero provides a straightforward method to ascertain whether the shaker is detached from the ground.

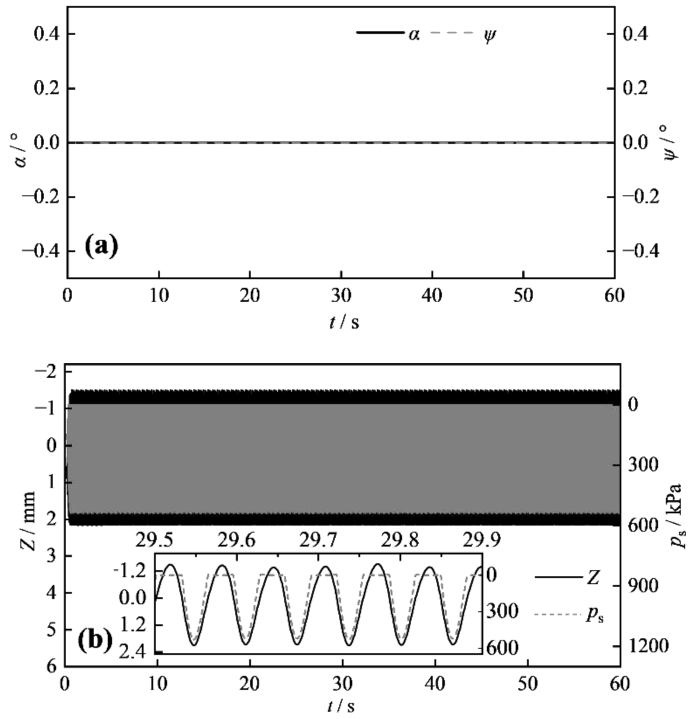

Fig. 10. System behavior of detached shaker with eccentric rotors synchronization: (a) α and ψ; (b) Z and p_s.

Changing n_e to 3 and f to 8 Hz, based on the Fig. 9 setup, and with initial conditions φ_1=−88° and φ_2=−92°, produces the dynamic profile in Fig. 11. Fig. 11a unveils a gradual escalation of the phase difference α, stabilizing at 180°. At this phase difference, the vertical and horizontal force components generated by each rotor cumulatively yield torques about the shaker's centroid. These torques induce rotational displacements in the ψ-direction, swinging between approximately −0.2° and 0.2°. If the excitation from the eccentric rotor is significantly amplified, desynchronization may induce substantial rotational displacements in the shaker, thereby elevating the risk of equipment tipping. Concurrently, α at 180° nullifies the vertical net force from the rotor excitations, culminating in Z and p_s of approximately 0.67 mm and 168 kPa, respectively—values in alignment with the corresponding values due to shaker's self-weight, as shown in Fig. 11b. Analysis of the shaker's dynamic behavior under these three operating conditions suggested that the mechanical design was likely effective for testing railway earthworks, provided that the shaker's two eccentric rotors were synchronized and the shaker remains grounded during operation.

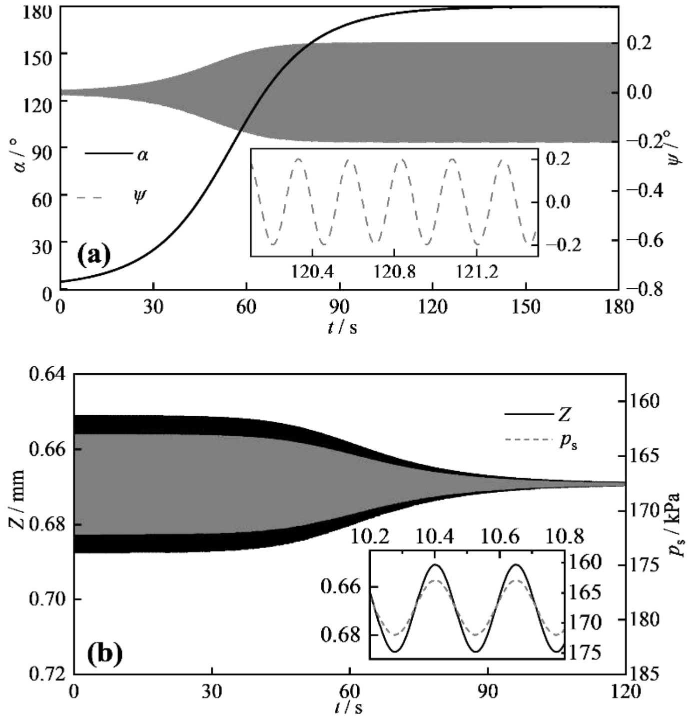

Fig. 11. System behavior during asynchronous rotation of eccentric rotors: (a) α and ψ; (b) Z and p_s.

4.3. Analysis of shaker performance under varied initial conditions

This section first examines the synchronization of the two eccentric rotors in the shaker under ideal conditions. However, field conditions may differ from the ideal conditions when applying to in-situ earthworks. Therefore, this section also analyses the effect of three variables: an initial phase difference in the eccentric rotors, inclined earthwork surfaces, and mass disparities in the shaker eccentric blocks. The foundation for all tests is characterized by k_f of 251.0 MPa/m and c_f of 868.3 kPa·s/m.

4.3.1 Ideal conditions

Fig. 12 presents the variation in the maximum absolute value of phase difference α_m of the eccentric rotors with respect to the motors' rotational frequency f' under ideal conditions. These observations are based on the last few tens of cycles during 180 s of operation when the shaker stays in contact with the ground. A larger α_m suggests reduced capacity for the eccentric rotor to sustain synchronous rotation in the given configuration. Here, ideal conditions refer to $\varphi_1=\varphi_2=-90°$ initially, $m_1=m_2$, and a horizontal foundation surface. In Fig. 12a, when $n_s=200$ and $n_e=1$, the maximum f' for the contact between shaker and foundation is 25 Hz. Increasing n_e to 4 and 10 results in a higher force due to increased rotor mass, which in turn lowers the maximum f' for the shaker in contact with the foundation to approximately 15.3 Hz and 11.5 Hz, respectively. Fig. 12b focuses on a configuration with $n_e=1$ and varying n_s values of 100, 152, and 176. The shaker remains attached to the ground. Importantly, under the ideal conditions illustrated in Fig. 12, the phase difference of the eccentric rotors consistently remains at zero, thereby sustaining synchronous operation.

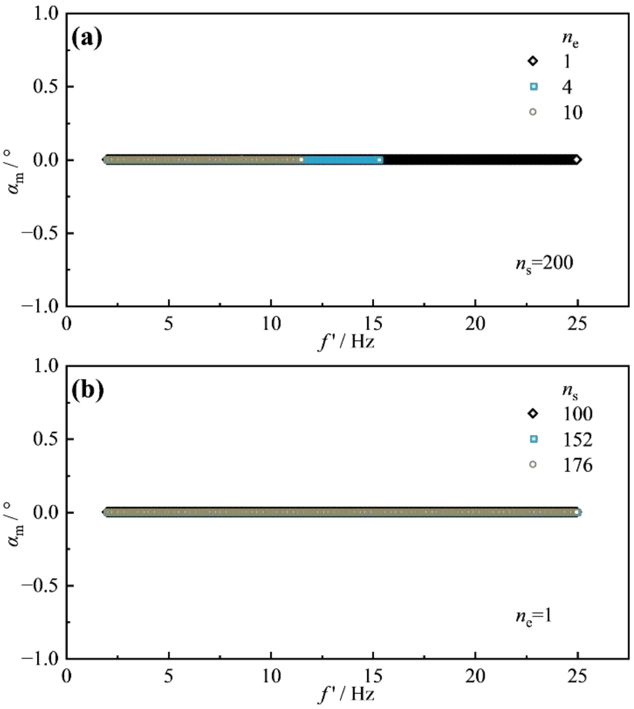

Fig. 12. Ideal operational state influences: (a) effect of n_e; (b) effect of n_s.

4.3.2 Initial rotor phase difference

Under initial conditions, the center of mass of the eccentric rotor may not align vertically with the motor shaft, posing challenges for precise adjustment. This scenario can be quantified in the dynamic model by considering an initial phase difference between the eccentric rotors. Based on the ideal condition, the initial phases of these rotors, represented as φ_1 and φ_2, are configured at −89° and −91°, respectively. The impact of a 2° initial phase difference on the relationship between α_m and f' is illustrated in Fig. 13. A comparison between Fig. 13 and Fig. 12 reveals that a minor initial phase difference does not affect the maximum f' for the contact between shaker and foundation. However, if f' falls below the natural frequency of 5.11 Hz associated with ψ-directed motion, α_m is magnified substantially, as shown in Fig. 13a. This indicates a poor synchronization of rotors. When f' is greater than 5.11 Hz, the system can adjust the phase difference to zero, thereby achieving automatic synchronization. Decreasing n_s to values of 100, 152, and 176, the natural frequency in ψ-directed motion increases to 5.79 Hz, 5.49 Hz, and 5.32 Hz, respectively. The variation in α_m for $n_e=1$ as a function of f' is depicted in Fig. 13b. This graph also indicates that self-synchronization of rotors is poor when f' is below the natural frequency related to ψ-directed motion. In conditions involving other frequencies, the system manages to nullify the phase difference of eccentric rotors.

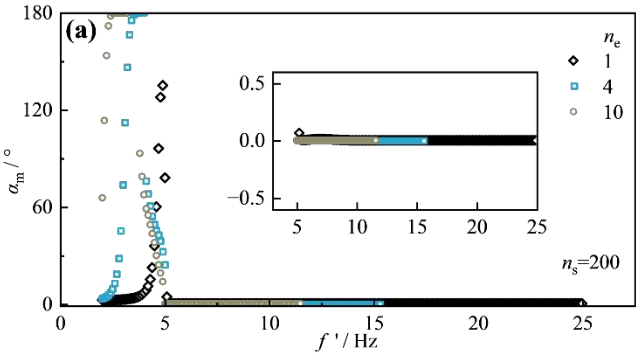

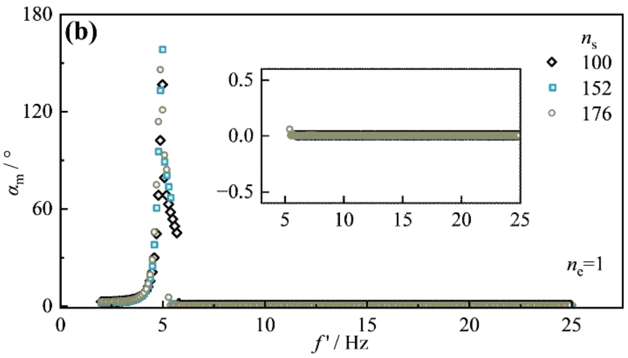

Fig. 13. Operational state with initial rotor phase difference: (a) effect of n_e; (b) effect of n_s.

4.3.3 Earthwork inclination

In the idealized condition, ψ was set to 0.5° initially to mimic an experimental scenario where the shaker's foundation surface exhibited a minor inclination. Fig. 14 illustrates how α_m varies with f' under these conditions of a slightly tilted foundation surface. A comparison between Fig. 14 and Fig. 12 reveals this minor inclination does not influence the maximum value of f' for the contact between shaker and foundation. Likewise, the phase difference between the two eccentric rotors is difficult to stabilize near a value of 0 when f' is below the natural frequency associated with ψ-directed motion, as shown in Fig. 14a. For a configuration where n_e=1, Fig. 14b presents the variation of α_m with f' when n_s sequentially decreases to 176, 152, and 100. The results indicate the eccentric rotors operate asynchronously when f' is marginally less than the natural frequency linked to ψ-directed motion. However, once f' decreases to approximately 4 Hz or lower, the rotor phase difference stabilizes close to 0, implying synchronisation.

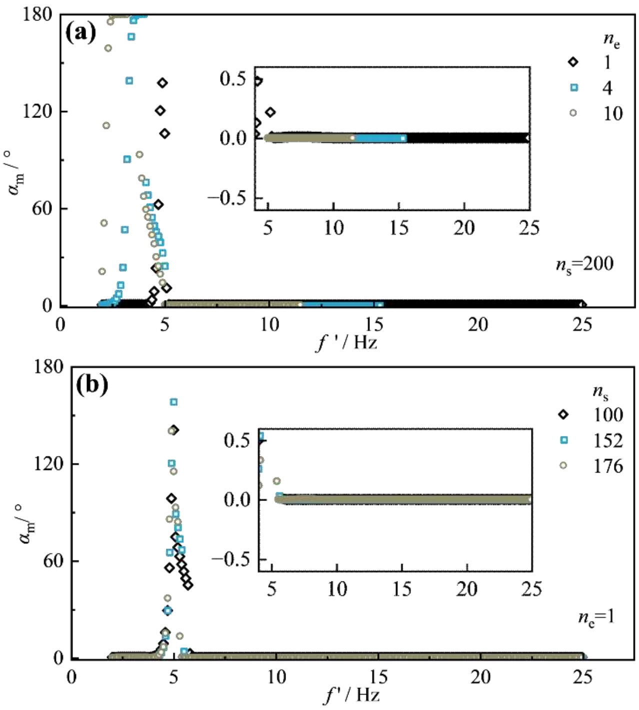

Fig. 14. Operational state on an inclined foundation: (a) effect of n_e; (b) effect of n_s.

4.3.4 Shaker mass discrepancies

Due to variations in machining accuracy, the dimensions of eccentric blocks can differ, leading to discrepancies in their mass. Under ideal conditions, the standard masses of the eccentric rotors, m_1 and m_2, were adjusted by −1.5% and +1.5% to account for these mass differences. Fig. 15 illustrates how α_m varies with f' when the masses of two eccentric rotors differ. A comparison of Fig. 15 with Fig. 12 reveals that mass discrepancies in the eccentric rotors do not affect the maximum value of f' without the shaker being detached from the foundation. However, small mass differences induce varying phase differences in the eccentric rotors, as shown in Fig. 15a. When f' is near or below the natural frequency associated with the shaker's ψ-directed motion, α_m is significantly larger, implying the phase difference of the eccentric rotors develops most rapidly. Conversely, if f ' exceeds this natural frequency, α_m remains small, indicating the eccentric rotors are approximately synchronous. Specifically, the smallest values of α_m occur when f' ranges between 6 Hz and 17 Hz. In the simulations corresponding to n_e=1 in Fig. 15a, varying n_s to 100, 152, and 176 respectively yielded the impact of f' on α_m as depicted in Fig. 15b. Similarly, it has been observed that α_m exhibits a notable increase when f' is marginally below the natural frequency associated with ψ-directed motion.

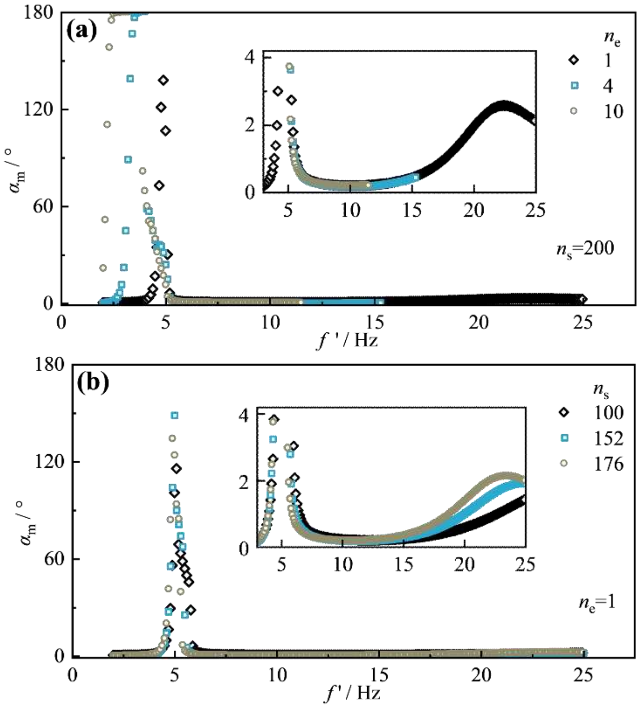

Fig. 15. Operational state with rotor mass discrepancies: (a) effect of n_e; (b) effect of n_s.

The simulations conducted in this section demonstrate the efficacy of the shaker design under idealized conditions. Moreover, these simulations indicated the mechanical design's potential applicability in non-idealized field conditions at frequencies f' above natural frequency linked to ψ-directed motion.

5. Field testing

This section begins with an overview of the shaker's manufacture. It then details a field calibration test on strongly weathered red-bed mudstone, aimed at assessing the shaker's performance across different configurations. Additionally, a method is introduced for estimating stiffness and damping coefficients in earthworks. Following this, an analysis of the test data in conjunction with simulations is provided.

It then concludes with a method for designing shaker configurations based on required loads.

5.1. Shaker manufacture

The components of the shaker depicted in Fig. 16 were machined according to the design illustrated in Fig. 7. The motors shown in Fig. 16a were secured using double rows of bolts on the internal frame positioned on the inside of the external frame in Fig. 16b. The double-layered circular loading plate, presented in Fig. 16c and d, was affixed to the bottom of the inner frame. During the experiments, the motor's power supply frequency was regulated using a frequency modulator depicted in Fig. 16e, connected to a 380 V, 50 Hz source. Additionally, Fig. 16f illustrates counterweight blocks, and Fig. 16g shows an eccentric block.

Fig. 16. Shaker components: (a) motors; (b) internal and external frame; (c) top view of the loading plate; (d) side view of loading plate; (e) frequency modulator; (f) counterweight blocks; (g) eccentric block.

5.2. Site condition and shaker setup

A calibration test was conducted near a railway line under construction, with earthworks consisting of strongly weathered red-bed mudstone. The strongly weathered mudstone in the vicinity of the test location had a upper crust thickness ranging from 10 to 13 cm, a density of 2080 kg/m³, and a moisture content between 6.2% and 10.4%. Additional properties included a modulus of subgrade reaction (K_{30}) ranging from 93.4 to 138.2 MPa/m and a saturated permeability coefficient of approximately 8.59×10^{-5} cm/s at a temperature of 20 °C. Beneath this crust lay weakly weathered red-bed mudstone. Fig. 17 illustrates the shaker during the in-situ calibration test. As depicted in Fig. 17a, a support structure, crafted from steel tubes, was erected to suspend a hoisting block. This block facilitated the lifting and positional adjustment of the shaker. Fig. 17b presents the fully assembled shaker. To inhibit relative displacement between the counterweights and the inner frame, wooden blocks were inserted into the gap.

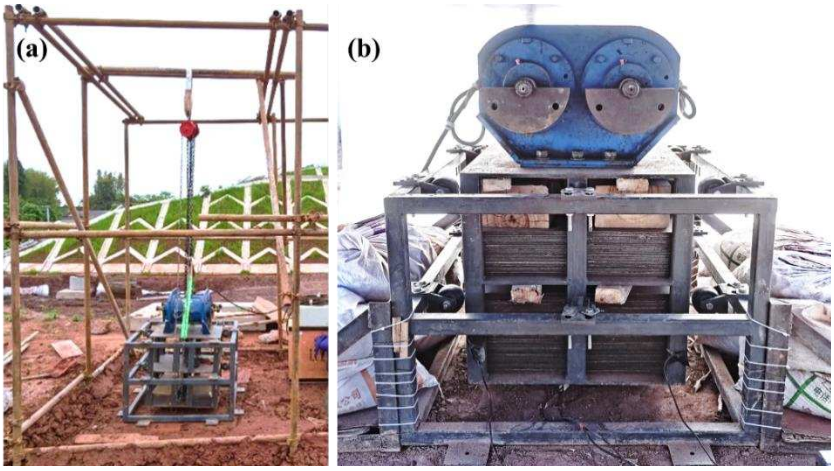

Fig. 17. Shaker at the test site: (a) shaker and lifting frames; (b) assembled shaker.

In the test, a force measurement system as depicted in Fig. 18 was employed to quantify the load exerted on the earthworks. This system includes a force-measuring device as shown in Fig. 18a and Fig. 18b, positioned between the loading plate and the ground, as well as a data acquisition instrument manufactured by the imc Test and Measurement GmbH and a microcomputer in Fig. 18c. The force-measuring device incorporates three load cells, evenly spaced at 120° intervals between two circular steel plates. These plates have a diameter of 300 mm and a thickness of 10 mm. The load cells, of type "QLMH-P", have specifications: height of 30 mm, diameter of 58 mm, capacity range of 2 t, accuracy of 0.3% F.S. (full scale), resolution of 0.1% F.S., and sensitivity of 2.0 mV/V. These load cells interface with the imc data collector and microcomputer to record the applied load from the shaker to the foundation. Prior to testing, the soil surface beneath the force-measuring device was leveled using sand, as shown in Fig. 18d.

Fig. 18. Force measurement system: (a) force-measuring device; (b) load cell configuration; (c) microcomputer and data acquisition instrument; (d) site levelling.

In the experiment, adjustments were made to the number of counterweight blocks (n_s), setting them sequentially to 100, 152, and 200. The number of eccentric blocks (n_e) at each motor end was set to 1, 2, 3, 4, 7, and 10 in sequence. Frequency sweep tests were conducted by incrementally enlarging the supply frequency (f) from 2 to 50 Hz for each combination of n_s and n_e. Observe the output load waveform on the microcomputer in real time. Following a period of stabilization of the shaker's output at the current frequency, adjust the frequency to the next level, with an increment of approximately 2.0 Hz. During actual operation, the equipment's operating status was also continuously monitored and a kill switch was available if the equipment showed signs of tipping or jumping.

5.3. Parameters estimation

Stiffness and damping of earthworks are important for analyzing the dynamic response of track-foundation systems under train loading [1,7,8]. Here, a straightforward method for estimating the stiffness coefficients (K_Z) and damping coefficients (C_Z) of soil based on field test data is proposed.

In cases of suboptimal synchronization between the eccentric rotors, the exciting force—measured when their phase difference has not fully developed—is regarded as the shaker's output. Under this condition, the two eccentric rotors rotate nearly in sync, allowing the shaker to ignore swing. Assuming equal mass for the eccentric rotors (m_1=m_2=m), the shaker model simplifies to a damped vibration system with single degree of freedom. This system is excited by a simple harmonic load, as depicted in Fig. 19, for which an analytical solution exists.

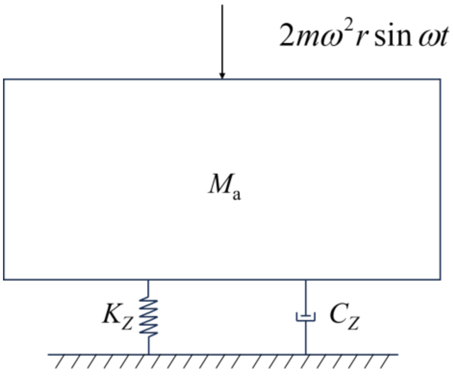

Fig. 19. Simplified vibration system diagram.

The stresses transmitted from the shaker to the underlying foundation comply with Eq. (36):

$$\begin{cases} p_{\text{p,v}} = (M_{\text{a}} g \pm 2\beta_{\text{a}} m\omega^2 r)/(\pi r_{\text{b}}^2) \\ p_{\text{p-v}} = 4\beta_{\text{a}} m\omega^2 r/(\pi r_{\text{b}}^2) \end{cases} \tag{36}$$

where p_p and p_v indicate the maximum and minimum values of the time-range curve of the stress exerted on the foundation by the shaker's loading plate, respectively. ω=$2\pi f'$ represents the angular frequency of the eccentric rotors. The peak-to-valley stress values, denoted as $p_\text{p-v}$, which indicate the difference between p_p and p_v, should not be greater than $2M_\text{a}g/(\pi r_\text{b}^2)$. The amplification factor, β_a, is analytically defined by Eq. (37):

$$\beta_{\mathrm{a}} = \frac{1}{\sqrt{[1-(\frac{\omega}{\sqrt{K_Z / M_{\mathrm{a}}}})^2]^2 + (\frac{\omega C_Z}{K_Z})^2}} \tag{37}$$

If the vibration of the shaker in the situ test is expressed as Fig. 19, both m and Ma in model can be measured using scales. The value of r is derived from the eccentric block's geometry, while ω is determined by the supply frequency. The variables K_Z and C_Z remain the only unknowns. However, the experimental relationship between β_{a} and ω can be derived from frequency-sweep vibration tests with shaker under specific configurations. The test value of β_{a} was determined as the ratio between the peak-to-valley value of the combined force measured beneath the loading plate and $4m\omega^2 r$. Moreover, Eq. (37) analytically expresses β_{a}, correlating it with ω, Ma, K_Z and C_Z. By keeping M_{a} consistent with test conditions, the analytical β_{a}-ω curves for certain set of K_Z and C_Z values may depict its experimental relationship. Optimization algorithms can be employed to find K_Z and C_Z values that best match the measured β_{a}-ω relationship, thereby defining the foundation's stiffness and damping coefficients. The objective function is determined as the coefficient of determination (R^2), indicating better agreement between the analytical and measured β_{a}-ω relationship as it approaches 1.0. Then, estimating the earthwork's stiffness and damping transforms into a mathematical challenge of identifying K_Z and C_Z values that maximize R^2 as calculated from Eq. (38) [42]:

$$R^2 = 1 - \frac{\sum_{i=1}^{N} (\beta_{\mathrm{a},\,i} - \hat{\beta}_{\mathrm{a},\,i}(K_Z,\ C_Z))^2}{\sum_{i=1}^{N} (\bar{\beta}_{\mathrm{a},\,i} - \hat{\beta}_{\mathrm{a},\,i}(K_Z,\ C_Z))^2} \tag{38}$$

where N denotes the number of samples of the data; $\beta_{\mathrm{a},\,i}$ represents the test value; $\hat{\beta}_{\mathrm{a},\,i}(K_Z,\ C_Z)$ denotes the estimated value determined using Eq. (37); $\bar{\beta}_{\mathrm{a},\,i}$ is the mean of the measured values.

Table 3 presents a set of test data for β_{a} and ω, as determined through frequency sweep tests on highly weathered red bedded mudstone. These tests used shaker settings of n_s=200 and n_e=2, yielding a M_a of 1205.3 kg. To derive the values for K_Z and C_Z, the flower pollination algorithm (FPA) [43,44] was applied, using data from Table 3. Key parameters for the FPA included a switch probability of 0.8, a population size of 20, and a scaling factor of 1×10^{-5} for the Lévy flight step size.

Table 3. The measured βa-ω relationship

f (Hz)	ω (rad/s)	βa	f (Hz)	ω (rad/s)	βa	f (Hz)	ω (rad/s)	βa	f (Hz)	ω (rad/s)	βa
8.07	25.35	1.07	20.16	63.33	1.19	31.83	100.00	2.01	46.25	145.30	1.47
10.18	31.98	1.11	22.20	69.74	1.22	34.08	107.07	2.43	46.55	146.24	1.38
11.94	37.51	1.11	24.14	75.84	1.29	36.02	113.16	2.59	48.50	152.37	1.30
14.12	44.36	1.07	26.10	82.00	1.35	40.56	127.42	2.10	50.00	157.08	1.07
16.24	51.02	1.23	28.16	88.47	1.48	42.50	133.52	1.84			
18.04	56.67	1.18	30.09	94.53	1.64	44.80	140.74	1.60			

Fig. 20 displays the iteration history of R^2 across five runs of FPA, revealing that the algorithm obtains a maximum R^2 value of 0.88 after less than 500 iterations. The values of K_Z and C_Z obtained from five runs show strong consistency after 1000 iterations. The mean values suggest K_Z and C_Z were 17.7 MN/m and 61.4 kN·s/m, respectively. In addition, according to Eq. (1), under the condition that the loading plate of the shaker is not separated from the ground, the resulting K_Z and C_Z ratios to the loading plate's bottom area represent the per unit area stiffness and damping, denoted by k_f and c_f, respectively. k_f is calculated at 251.0 MPa/m and c_f at 868.3 kPa·s/m.

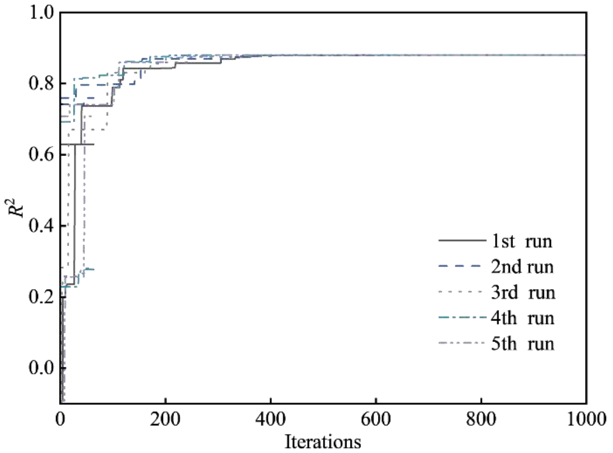

Fig. 20. Iteration histories of R^2.

The ease and accuracy of the shaker's self-weight calculation allow for checking the suitability of Eq. (36) in estimating the shaker's output via verifying the $p_{\text{p-v}}$ equation. Additionally, $p_{\text{p-v}}$ correlates with β_a, which is derived from K_Z and C_Z, among others. Therefore, this process also verifies the validity of the K_Z and C_Z values derived from the estimation. Fig. 21 presents a comparison of the tested and estimated values of $p_{\text{p-v}}$ derived from various conditions, characterized by differing values of n_s and n_e in frequency sweep test. It is observed that the estimated values are marginally lower than the tested values at higher load values. Overall, the data points are closely aligned with the 1:1 line, demonstrating a significant consistency between the estimated and experimental values. This alignment substantiates the reliability of Eq. (36) and the estimation method used for K_Z and C_Z.

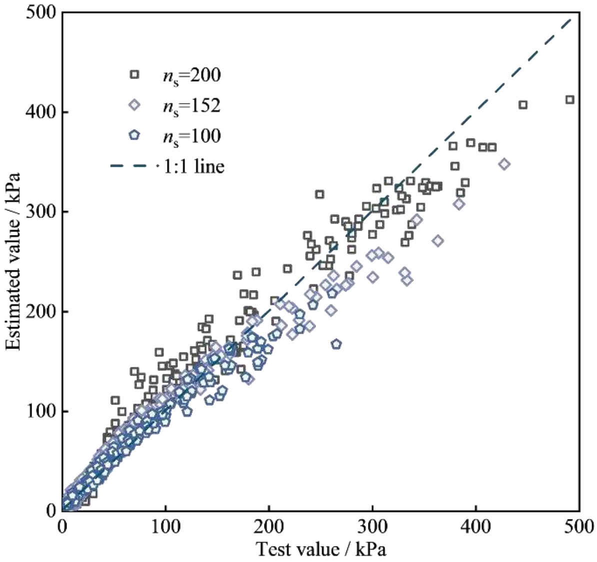

Fig. 21. Estimated vs. measured $p_{\text{p-v}}$ comparison.

5.4. Results and interpretation

Fig. 22 presents the time-history of stress p_s exerted on the foundation surface by the shaker during the system's stable phase. The time variable (t) depicted in the figures signifies the relative time difference rather than the actual operational duration of the system. In Fig. 22a, with n_s=100, n_e=4, and supply frequency f of 13.84 Hz, the maximum value of p_s reaches approximately 125 kPa, while the minima is approximately 90 kPa. The corresponding loading frequency is approximately 7 Hz. The discrepancy between the simulation and experimental data for the maximum and minimum values of p_s remains within a 5% margin, and the frequencies are essentially identical. Alternatively, for f of 20.19 Hz, the time-dependent profile of p_s is depicted in Fig. 22b. The maximum and minimum values of p_s are approximately 150 kPa and 64 kPa, respectively, with f' approximately 10 Hz. Once again, the simulation data aligns well with the experimental findings.

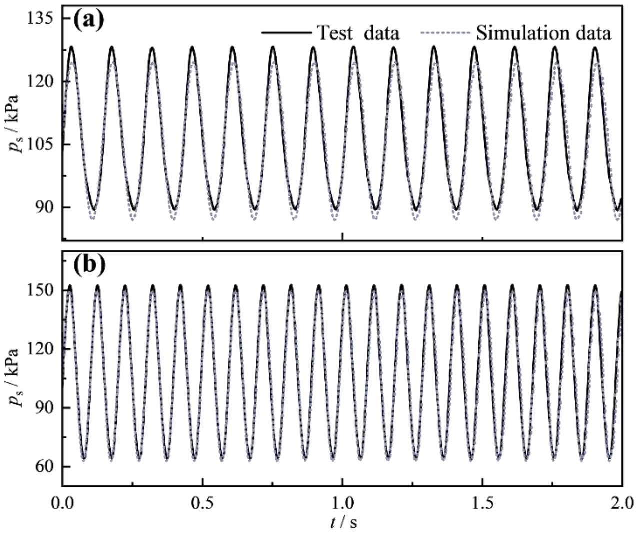

Fig. 22. Time-dependent stress response analysis: (a) n_s=100, n_e=4, f= 13.84 Hz; (b) n_s=100, n_e=4, f= 20.19 Hz.

The experimental test data and simulation data of stresses applied to the foundation surface by the shaker with varying n_s and n_e are compared in Fig. 23. The data in these figures pertain to conditions where the shaker remains attached to the foundation. Data pertaining to certain conditions involving poorly synchronized eccentric rotors were obtained during intervals when the phase difference between the two rotors had not yet fully evolved. Fig. 23a illustrates the relationship between the stress minima

(p_v) and the eccentric rotors' rotation frequency (f') for varying n_e with n_s set at 100. For Z-directed motion, the natural frequency of the system is approximately 24.48 Hz. Typically, f' is lower than this natural frequency. As f' or n_e increases, the excitation from the rotating eccentric rotors intensifies, resulting in a decrease in p_v. The simulated and field values of p_v exhibit strong consistency. The experimental maximum value of f' in scenarios where the shaker is in constant contact with foundation is marginally smaller than the simulated value. This discrepancy can be attributed to the early termination of the test, which was necessitated by instability issues arising from an inadequate shaker counterweight as p_v approached zero. When n_s is adjusted to 200, Fig. 23b displays the correlation between p_v and f'. Again, a strong correlation between simulated and experimental data is observed. It can also be observed that the trend of p_v shifts from decreasing to increasing as f' increases for configurations where n_e is either 1 or 2 and f' exceeds the natural frequency for Z-directed motion (approximately 19.34 Hz).

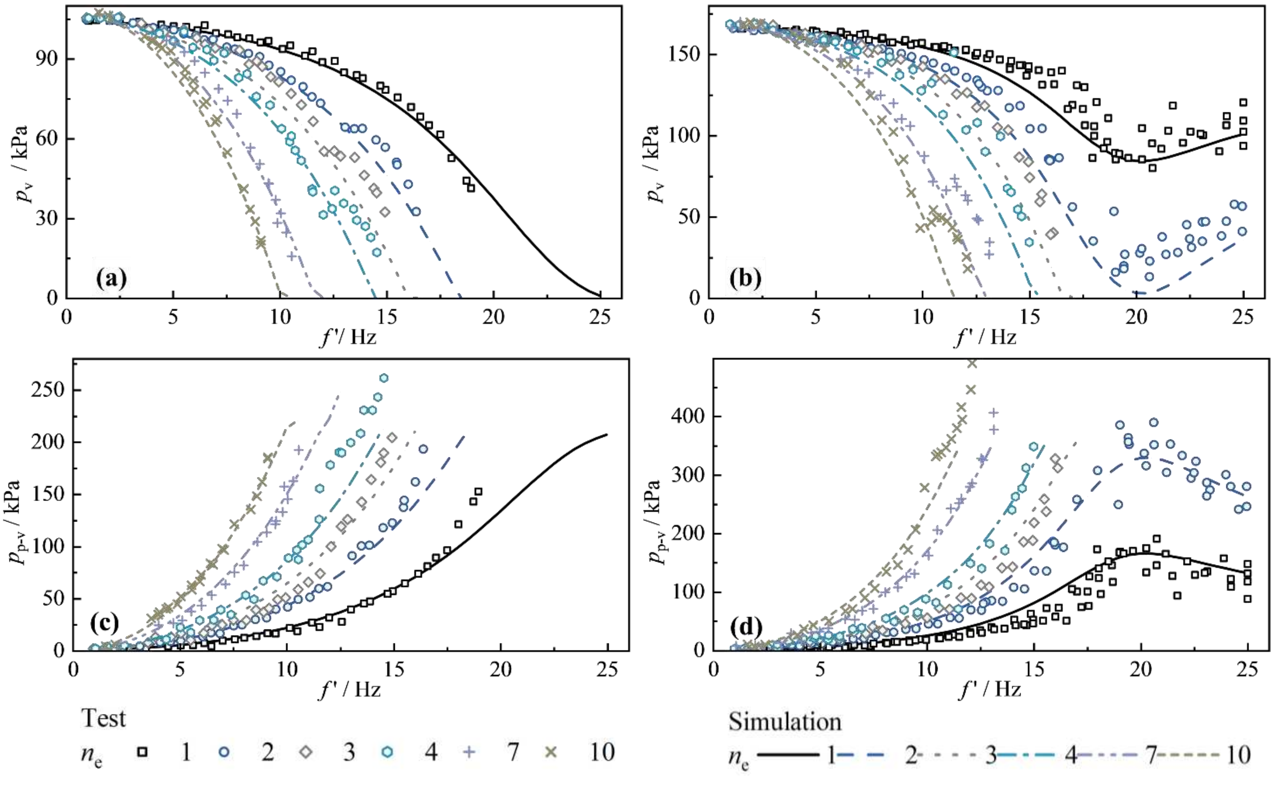

Fig. 23. Foundation stress profiles by shaker: (a) p_v at n_s=100; (b) p_v at n_s=200; (c) $p_{p\text{-}v}$ at n_s=100; (d) $p_{p\text{-}v}$ at n_s=200

Fig. 23c and Fig. 23d illustrate the relationship between peak-to-valley values ($p_{p\text{-}v}$) of stress and rotation frequency (f') of eccentric rotors for n_s of 100 and 200, respectively. When f' is lower than the natural frequency, an increase in f' or n_e amplifies the excitation generated by the eccentric rotors' rotation, subsequently increasing $p_{p\text{-}v}$. Conversely, when f' exceeds the natural frequency, $p_{p\text{-}v}$ reduces as f' increases. Furthermore, Fig. 23c and Fig. 23d also confirm the close alignment between simulated and experimental $p_{p\text{-}v}$ values.

The phases of the eccentric rotors considering n_s=200 and n_e=1 are depicted in Fig. 24. During several moments corresponding to f'=3.52 Hz in Fig. 24a, the eccentric rotors demonstrate asynchronous operation. Concurrently, the shaker exhibits swinging behavior that aligns with the direction of ψ in the aforementioned mathematical model. Contrastingly, at f'=12.36 Hz, shown in Fig. 24b, the phases of the eccentric rotors appear consistent. Under these conditions, the shaker operates without swinging. However, poor synchronization of the eccentric rotors occurs again at f'=23.40 Hz, as indicated in Fig. 24c, accompanied by a minor swing in the shaker. Of particular note is the significant swing of the shaker when f' approaches 5 Hz. Under these conditions the experiment was terminated to prevent equipment tipping. Alternatively, the supply frequency should be rapidly elevated before the phase difference of the eccentric rotors is sufficiently developed. Moreover, observations from experimental phenomena indicate optimal stable operation of the shaker occurs when eccentric rotors' rotational frequency f' lies within the range of approximately 6 to 16 Hz. These observations align with the simulation analysis presented in Section 4.3.

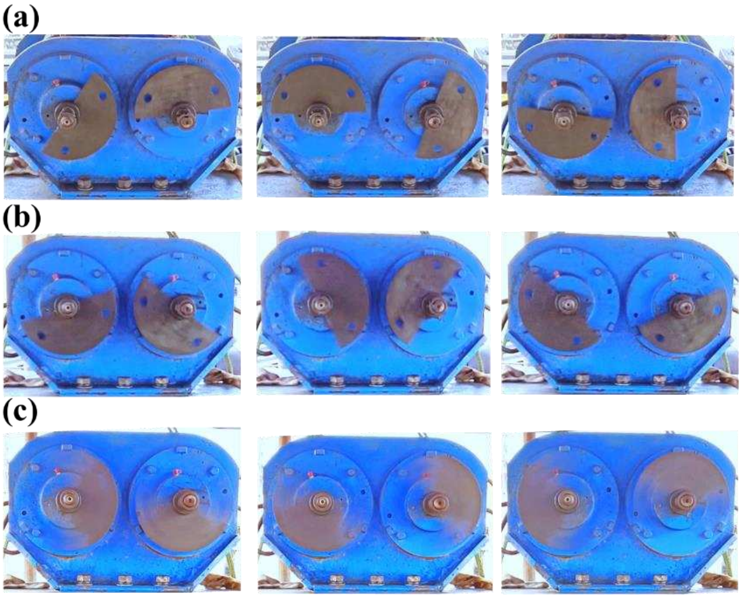

Fig. 24. Eccentric block phasing at differing frequencies: (a) f'= 3.52 Hz; (b) f'=12.36 Hz; (c) f'=23.40 Hz.

5.5. Configuration design

To enhance experimental efficiency and reduce the costs of sensor usage in the cumulative settlement test over a long period of time, it is suggested to conduct frequency sweep tests on the earthworks to be evaluated. These tests serve the purpose of assessing the stiffness and damping properties of the earthworks, providing estimations for the shaker's output load without the use of load cells. Subsequently, the shaker configuration can be adjusted to produce the requisite force according to the output stress characteristics. This process determines shaker configuration including the number of eccentric blocks (n_e) at each end of the shaker motor, the total count of counterweight blocks (n_s), and the supply frequency (f). Output stress characteristics determined by train loading include the minimum value (p_v), the peak-to-valley value ($p_{p\text{-}v}$) and the frequency. The frequency could be regarded as the rotational frequency (f') of the motors. The procedure of configuration design is illustrated in Fig. 25 and consists of the following steps:

Step 1: Input. Specify the desired stress characteristics p_v, $p_{p\text{-}v}$, and f', along with other known parameters such as K_Z, C_Z, r, r_b, m_e, m_s, and g.

Step 2: Determination of $\boldsymbol{n_e}$. After calculating ω and M_a from the provided parameters, the amplification factor (β_a) is derived from Eq. (37). Subsequently, the desired value of n_e is obtained from the second equation in Eq. (36) and Eq. (17). Notably, n_e should be adjusted to a positive integer closest to the calculated value.

Step 3: Determination of $\boldsymbol{n_s}$. By subtracting the mass of the eccentric blocks and any other masses not included in the counterweight blocks from M_a, the desired mass of the counterweight blocks (M_s) is established. M_s is then divided by the mass of individual counterweight blocks (m_s) to ascertain n_s. For better stability of the shaker, the counterweight blocks should be stacked at the same height. Hence, it is recommended to adjust n_s to a multiple of 4 closest to the calculated value.

Step 4: Determination of $\boldsymbol{f}$. For vibration motors equipped with two pole pairs, the required supply frequency f is approximately twice the value of f'.

Step 5: Output. Numerical simulation is employed to assess whether the obtained values of n_e, n_s, and f fall within the applicable range of the shaker. Finally, output recommendations for configuration.

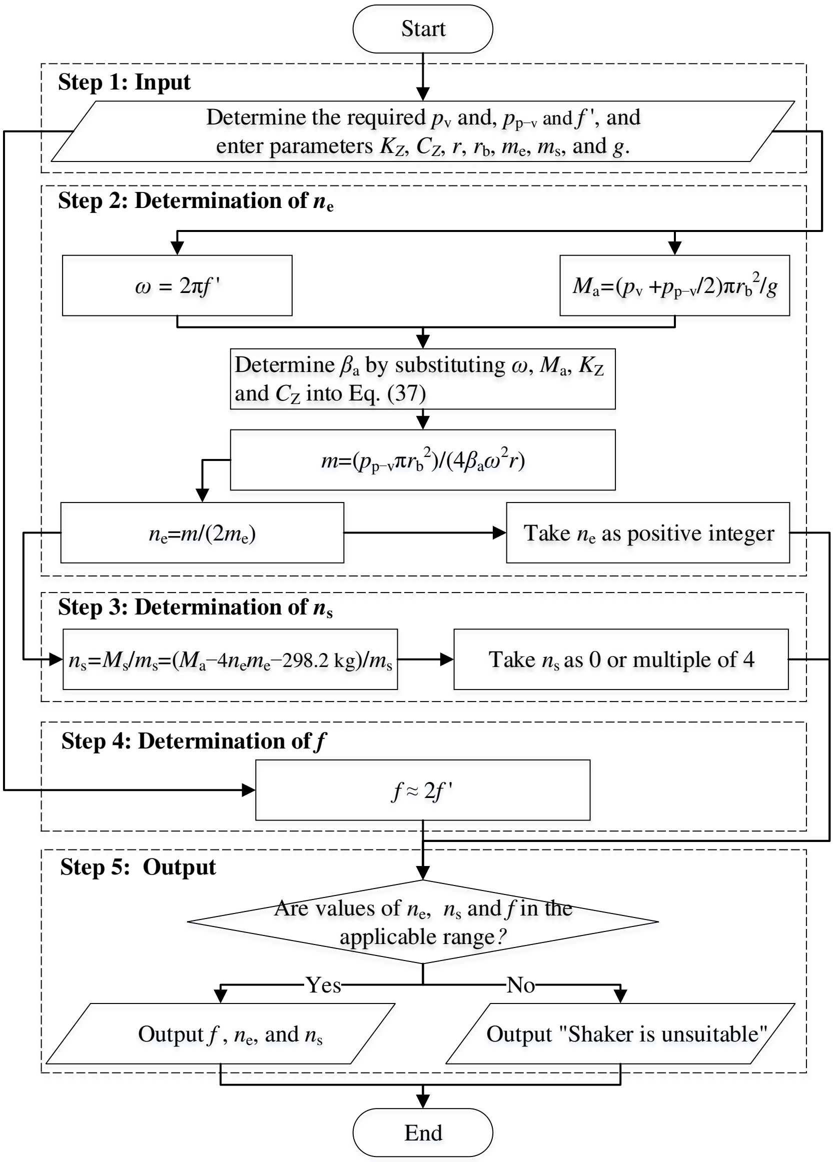

Fig. 25. Flowchart for configuration design of shaker.

In a site comparable to the study area, this method determined that a configuration with $n_e = 4$, $n_s = 60$, and $f = 22$ Hz would produce dynamic stress ranging from 30 to 130 kPa at 11 Hz. This stress magnitude approximately aligns with that experienced in ballast track foundations under train loading. Furthermore, a configuration with $n_e = 1$, $n_s = 0$, and $f = 22$ Hz would produce stress values between 30 and 53 kPa at 11 Hz, approximately replicating the stress range of slab track foundations.

6. Conclusions

Understanding the mechanical performance of track earthworks is important for the construction, operation, and maintenance of railways. To assist with this, a earthworks shaker was developed. First the design requirements were outlines, followed by the development of a conceptual model to describe the shaker operation. Using the model, virtual development of the shaker was undertaken to determine the effect of different factors. Lastly, the shaker was constructed and tested on a railway construction site. The conclusions were:

(1) The shaker is suitable for studying earthworks. Data from frequency sweep tests aid in estimating the stiffness and damping coefficients of earthworks. Field tests on a weathered red-bed mudstone with a modulus of subgrade reaction (K_{30}) ranging from 93.4 to 138.2 MPa/m showed a stiffness coefficient of 251.0 MPa and damping coefficient of 868.3 kPa·s/m. Furthermore, by adjusting the shaker configuration, it is possible to generate dynamic loads that mimic the stress magnitudes of track foundation under train loading.

(2) The proposed dual-rotor shaker is a novel design compared to current railway earth dynamic test shakers. Its uniqueness stems from the lack of mechanical coupling between the two eccentric rotors. This eliminates the need for a cooling system to cool the connecting mechanism, thereby enhancing economic efficiency in operation and maintenance.

(3) The phase synchronization between the shaker’s two eccentric rotors is influenced by potential mass discrepancies and initial conditions. Even minor deviations from these conditions may adversely affect synchronization. This issue becomes particularly problematic when the rotational frequency of rotors is near or below the system’s natural frequency associated with swinging motion, resulting in shaker oscillations. Simulations and field tests reveal that, within a rotational frequency range of 6 to 16 Hz, the shaker's eccentric rotors synchronize effectively, ensuring stable loading output.

It is important to note that the proposed shaker encounters challenges in accurately replicating the stresses induced in railway earthwork by train loading. Moreover, the correlation between the frequency of simple harmonic loading and train-induced loading needs to be further explored. To address these shortcomings, it is advisable to establish cumulative settlement thresholds. These thresholds should be defined by subjecting the inertial shaker to railway earthworks already in practical use and proven to meet usage requirements. When assessing soil in railway earthworks, the settlement should not exceed this threshold under the same loading conditions. Adhering to this standard allows for the better application of inertial shakers in the quantitative evaluation of railway earthworks.

Data availability statement

All data, models, and code generated or used during the study appear in the submitted article.

Acknowledgments

This research was funded by the National Natural Science Foundation of China (Grant No. 52078435), the Natural Science Foundation of Sichuan Province (Grant No. 2023NSFSC0391), the Overseas Expertise Introduction Project for Discipline Innovation ("111 Project ", Grant No. B21011), and the Royal Society UK (IEC\NSFC\211306). We extend our gratitude to Mr. Jianxiang Zhou for his invaluable assistance during the field trials.

References

[1] Guo Y, Zhai W, Sun Y. A mechanical model of vehicle-slab track coupled system with differential subgrade settlement. Structural Engineering and Mechanics 2018;66:15–25. https://doi.org/10.12989/SEM.2018.66.1.015.

[2] Feng G, Zhang L, Luo Q, Wang T, Xie H. Monitoring the dynamic response of track formation

with retaining wall to heavy-haul train passage. International Journal of Rail Transportation 2022:1–19. https://doi.org/10.1080/23248378.2022.2103849.

[3] Luo Q, Fu H, Liu K, Wang T, Feng G. Monitoring of train-induced responses at asphalt support layer of a high-speed ballasted track. Construction and Building Materials 2021;298:123909. https://doi.org/10.1016/j.conbuildmat.2021.123909.

[4] Mei H, Leng W, Nie R, Tu R, Li Y, Dong J. Experimental research on the dynamic response characteristics of the transition subgrade induced by heavy-haul train passage. Proceedings of the Institution of Mechanical Engineers, Part F: Journal of Rail and Rapid Transit 2019;233:974–87. https://doi.org/10.1177/0954409718822924.

[5] Zhai W, Wang K, Chen Z, Zhu S, Cai C, Liu G. Full-scale multi-functional test platform for investigating mechanical performance of track–subgrade systems of high-speed railways. Rail Eng Science 2020;28:213–31. https://doi.org/10.1007/s40534-020-00221-y.

[6] Indraratna B, Ngo T, Ferreira FB, Rujikiatkamjorn C, Tucho A. Large-scale testing facility for heavy haul track. Transportation Geotechnics 2021;28:100517. https://doi.org/10.1016/j.trgeo.2021.100517.

[7] Zhai W, Wang K, Cai C. Fundamentals of vehicle–track coupled dynamics. Vehicle System Dynamics 2009;47:1349–76. https://doi.org/10.1080/00423110802621561.

[8] Xie H, Luo Q, Wang T, Jiang L, Connolly DP. Stochastic analysis of dynamic stress amplification factors for slab track foundations. International Journal of Rail Transportation 2023:1–23. https://doi.org/10.1080/23248378.2023.2170286.

[9] Cai X, Zhang Q, Wang Q, Cui X, Dong B. Effects of the subgrade differential arch on damage characteristics of CRTS III slab track and vehicle dynamic response. Construction and Building Materials 2022;327:126982. https://doi.org/10.1016/j.conbuildmat.2022.126982.

[10] Ye Q, Luo Q, Connolly DP, Wang T, Xie H, Ding H. The effect of asphaltic support layers on slab track dynamics. Soil Dynamics and Earthquake Engineering 2023;166:107771. https://doi.org/10.1016/j.soildyn.2023.107771.

[11] Jiang H, Li Y, Wang Y, Yao K, Yao Z, Xue Z, et al. Dynamic performance evaluation of ballastless track in high-speed railways under subgrade differential settlement. Transportation Geotechnics 2022;33:100721. https://doi.org/10.1016/j.trgeo.2022.100721.

[12] Wang L. Vibration characterization of fully-closed high speed railway subgrade through frequency: Sweeping test. Soil Dynamics and Earthquake Engineering 2016;88:33–44. https://doi.org/10.1016/j.soildyn.2016.05.011.

[13] Wang L, Lei X, Liu S. Investigation of immersion influence on dynamic properties of high-speed railway subgrade with semi-rigid waterproof functional layer through field-excitation testing. Can Geotech J 2018;55:19–33. https://doi.org/10.1139/cgj-2016-0606.

[14] Esen AF, Woodward PK, Laghrouche O, Connolly DP. Stress distribution in reinforced railway structures. Transportation Geotechnics 2022;32:100699. https://doi.org/10.1016/j.trgeo.2021.100699.

[15] Marolt Čebašek T, Esen AF, Woodward PK, Laghrouche O, Connolly DP. Full scale laboratory testing of ballast and concrete slab tracks under phased cyclic loading. Transportation Geotechnics 2018;17:33–40. https://doi.org/10.1016/j.trgeo.2018.08.003.

[16] Bian X, Jiang H, Cheng C, Chen Y, Chen R, Jiang J. Full-scale model testing on a ballastless

high-speed railway under simulated train moving loads. Soil Dynamics and Earthquake Engineering 2014;66:368–84. https://doi.org/10.1016/j.soildyn.2014.08.003.

[17] Miwa M, Yoshimura A. Study on vertical dynamic vehicle-track interactions using the TRADYS test facility and computer simulation. Computers in Railways X, vol. 1, Prague, Czech Republic: WIT Press; 2006, p. 885–94. https://doi.org/10.2495/CR060861.

[18] Huang J, Su Q, Liu T, Wang X. Vibration and long-term performance analysis of pile-plank-supported low subgrade of ballastless track under excitation loads. Shock and Vibration 2015;2015:1–12. https://doi.org/10.1155/2015/404627.

[19] Efthymiou G, Vrettos C. Kinematic response of pile groups and piled rafts to a distant stationary or moving harmonic load via the FEM. Soil Dynamics and Earthquake Engineering 2024;176:108264. https://doi.org/10.1016/j.soildyn.2023.108264.

[20] Liu H, Luo Q, El Naggar MH, Zhang L, Wang T. Centrifuge modeling of stability of embankment on soft soil improved by rigid columns. J Geotech Geoenviron Eng 2023;149:04023069. https://doi.org/10.1061/JGGEFK.GTENG-11314.

[21] Zhang C, Jiang G, Buzzi O, Su L. Full-scale model testing on the dynamic behaviour of weathered red mudstone subgrade under railway cyclic loading. Soils and Foundations 2019;59:296–315. https://doi.org/10.1016/j.sandf.2018.11.007.

[22] Cai Y, Xu L, Liu W, Shang Y, Su N, Feng D. Field Test Study on the dynamic response of the cement-improved expansive soil subgrade of a heavy-haul railway. Soil Dynamics and Earthquake Engineering 2020;128:105878. https://doi.org/10.1016/j.soildyn.2019.105878.

[23] Ye Y-S, Lou L-W, Cai D-G, Shi Y-F, Yan H-Y, Wei S-W. Mechanical properties of track-asphalt concrete-subgrade bed structure system under both temperature and train loading. Construction and Building Materials 2022;340:127556. https://doi.org/10.1016/j.conbuildmat.2022.127556.

[24] Hou Y, Peng H, Fang P, Zou M. Synchronous characteristic of three homodromy motors in vibrating isolation system. J Mech Sci Technol 2021;35:45–60. https://doi.org/10.1007/s12206-020-1204-2.

[25] Zhang X, Yue H, Li Z, Xu J, Wen B. Stability and coupling dynamic characteristics of a vibrating system with one internal degree of freedom and two vibrators. Mechanical Systems and Signal Processing 2020;143:106812. https://doi.org/10.1016/j.ymssp.2020.106812.

[26] Cieplok G, Wójcik K. Conditions for self-synchronization of inertial vibrators of vibratory conveyors in general motion. Journal of Theoretical and Applied Mechanics 2020;58:513–24. https://doi.org/10.15632/jtam-pl/119023.

[27] Zhang X, Zhang X, Hu W, Zhang W, Chen W, Wang Z, et al. Theoretical, numerical and experimental studies on multi-cycle synchronization of two pairs of reversed rotating exciters. Mechanical Systems and Signal Processing 2022;167:108501. https://doi.org/10.1016/j.ymssp.2021.108501.

[28] Zhang X, Zhang X, Zhang C, Wang Z, Wen B. Double and triple-frequency synchronization and their stable states of the two co-rotating exciters in a vibrating mechanical system. Mechanical Systems and Signal Processing 2021;154:107555. https://doi.org/10.1016/j.ymssp.2020.107555.

[29] Liu L, Liu T, Yue H, Zhang X. Coupling synchronization principle of two pairs counter-rotating unbalanced rotors in the different resonant conditions. Journal of Low Frequency Noise, Vibration and Active Control 2021;40:1149–65. https://doi.org/10.1177/1461348420937887.

[30] Zhang X, Wen B, Zhao C. Vibratory synchronization transmission of two exciters in a super-resonant vibrating system. J Mech Sci Technol 2014;28:2049–58. https://doi.org/10.1007/s12206-014-0108-4.

[31] Zhou Z. Experiment and numerical simulation of the dynamic response of subgrade bed in the Wu-Guang passenger railline. Master Thesis. Central South University, 2010.

[32] Feng G, Luo Q, Wang T, Connolly DP, Liu K. Frequency spectra analysis of vertical stress in ballasted track foundations: influence of train configuration and subgrade depth. Transportation Geotechnics 2024;44:101167. https://doi.org/10.1016/j.trgeo.2023.101167.

[33] Hu J, Bian X. Analysis of dynamic stresses in ballasted railway track due to train passages at high speeds. J Zhejiang Univ Sci A 2022;23:443–57. https://doi.org/10.1631/jzus.A2100305.

[34] Wang Z, Jiang G, Wei Y, Hu A. Experimental study of cyclic loading for subgrade bed of high speed railway. Rock and Soil Mechanics 2010;31:760–4. https://doi.org/10.16285/j.rsm.2010.03.015.

[35] Bian X, Li W, Hu J, Liu H, Duan X, Chen Y. Geodynamics of high-speed railway. Transportation Geotechnics 2018;17:69–76. https://doi.org/10.1016/j.trgeo.2018.09.007.

[36] Zhang X. Numerical simulation and experiment study on macro-meso mechanical behaviors of high-speed railway ballast. Doctor Thesis. Southwest Jiaotong Univ., 2012.

[37] Zhai W-M. Two simple fast integration methods for large-scale dynamic problems in engineering. Int J Numer Meth Engng 1996;39:4199–214. https://doi.org/10.1002/(SICI)1097-0207(19961230)39:24<4199::AID-NME39>3.0.CO;2-Y.

[38] Zhai W. Vehicle–track coupled dynamics: theory and applications. Singapore: Springer Singapore; 2020. https://doi.org/10.1007/978-981-32-9283-3.

[39] Zou M, Fang P, Hou Y, Peng H, Wang D. Study on synchronization mechanism and experiment of vibrating system actuated with double-frequency and dual-rotor. Chinese Journal of Theoretical and Applied Mechanics 2021;53:2823–40. https://doi.org/10.6052/0459-1879-21-359.

[40] Li Y, Li H, Wei X, Wen B. Self-synchronization theory of a nonlinear vibration system driven by two exciters. Part 1: Theoretical analysis. Journal of Vibroengineering 2014;16:725–34.

[41] Tang J, Liu R. Motors and Drags. 3rd ed. Beijing: Higher Education Press; 2014.

[42] Chen W, Ding J, Wang T, Ying Z, Wan X. An adaptive sequential sampling method based on ANN_MCD and RF: Application in geotechnical problems. Applied Soft Computing 2023:110462. https://doi.org/10.1016/j.asoc.2023.110462.

[43] Lyu P, Luo Q, Wang T, Connolly DP. Railway gravity retaining wall design using the flower pollination algorithm. Transportation Geotechnics 2023;42:101065. https://doi.org/10.1016/j.trgeo.2023.101065.

[44] Yang XS. Flower pollination algorithm for global optimization. Unconv Comput Nat Comput 2012;7445:240–9.